Kinetics and Cellular Viability of Needle and Needle-free Liquid Jet Injection (NFLJI)

Madeleine Liblong

Master of Engineering

Supervised by Prof. Luc Mongeau

Department of Biological and Biomedical Engineering McGill University
Montreal, Québec

2024-04-15

A thesis submitted to McGill University in partial fulfillment of the requirements of the degree of Master of Engineering.

Copyright © Madeleine Liblong, 2024

I TABLE OF CONTENTS

II ABSTRACT

It is reported that up to 9% of the population suffers from a voice dysfunction or disorder at some point in their lives. Voice disorders may occasionally require treatment through the injection of biomaterials, such as collagen or fat, to the lamina propria. Limitations in the conventional use of needles for this application offers an opportunity for the adaptation of needle-free liquid jet injection (NFLJI). Recent work has highlighted benefits of NFLJI in terms of reduced experiences of needle phobia and pain. However, there remains a lack of understanding regarding tissue response to NFLJI, preventing their wider use today.

The present study compared the kinetics and cellular viability of needle and needle-free injection. In order to do so, a PPG hydrogel was developed as a phantom to study injection mechanics in-vitro. The PPG material was formulated using three different PEGDA compositions. The mechanical properties of each gel composition were measured and matched to those of native vocal fold tissue. The PPG composition most closely replicating native vocal fold tissue was then selected and subject to both needle injection and NFLJI at varying injection parameters. Needle injection parameters included the insertion rate, the injection rate, liquid volume, and needle gauge. Needle-free injector parameters included driving pressure and liquid volume. The dynamic, morphological, and biological response elicited by each injection within the scaffold was compared.

Results showed that all hydrogel compositions broadly met target elastic modulus values, with the 10% and 30% PEG composition hydrogels matching the fracture toughness and storage modulus of the lamina propria. The 30% gel composition was ultimately selected based on its more realistic

dispersion profile and enhanced porosity. The results showed that needle geometry and scaffold structure influenced the deformation and frictional forces associated with needle insertion. The overall peak force generated by needle injection was greater than that produced by needle insertion. It was found that the average force and duration of needle-free injection were 18x larger and 20x smaller than the values for needle injection, respectively. Needle injection was characterized by individual periods of needle insertion, injection, and removal while NFLJI was characterized by a high amplitude vibration that decayed exponentially. After the initial impact, morphological results showed that the average depth and width of NFLJI was 1.9x and 1.7x greater than those from needle injection. The needle injection bolus expanded radially from the needle tip while the bolus from NFLJI injection expanded vertically along a long shaft.

Variation in experimental parameters resulted in changes in the force, duration, width, and depth associated with each injection technique. Finally, preliminary results showed that the cell viability of needle injection was 1.1 times greater than NFLJI. Needle-free injection created a significantly larger material void than needle injection, indicating that injection force was proportional to tissue damage and deformation. Needle injection was concluded to be a gentler technique for vocal fold drug delivery. The increased duration and reduced force of needle injection allowed for a superficial injection to be reliably delivered with minimal tissue damage. Although the decreased duration and increased depth of NFLJI likely contributed to the reduced pain and occasional bleeding experienced with this technique, the force and injection width of NFLJI should be reduced to improve its clinical implementation.

III ABREGE

On estime que jusqu'à 9 % de la population souffre d'un trouble de la voix à un moment ou à un autre dens les vie. Les troubles de la voix peuvent parfois nécessiter un traitement par injection de biomatériaux, tels que le collagène ou la les lipides, dans la lamina propria. Cette application offer une possibilité d'adapter l'injection de liquide sans aiguille (NFLJI). Des travaux récents ont mis en évidence les avantages de l'INFLJ en termes de réduction de la phobie de l'aiguille et de la douleur. Cependant, la réponse des tissus à l'INFLJ reste mal comprise, ce qui limite son utilisation à grande échelle.

La présente étude a comparé la cinétique de l'injection avec et sans aiguille. Pour ce faire, un hydrogel PPG a été développé comme fantôme pour étudier les mécanismes d'injection in vitro. Le matériau PPG a été formulé à partir de trois compositions différentes de PEGDA. Les propriétés mécaniques de chaque composition de gel ont été mesurées et comparées à celles du tissu des cordes vocales. L'échafaudage PPG sélectionné a ensuite été soumis à l'injection à l'aiguille et à la NFLJI pour différents paramètres d'injection. Les paramètres de l'aiguille comprenait le taux d'insertion, le taux d'injection, le volume de liquide et le calibre de l'aiguille. Les paramètres de l'injecteur sans aiguille incluent la pression d'entraînement et le volume de liquide. La réponse dynamique, morphologique et biologique provoquée par chaque injection dans l'échafaudage a été comparée.

Les résultats ont montré que toutes les compositions d'hydrogel atteignaient largement les valeurs cibles de module élastique, Les hydrogels à 10 % et 30 % de composition PEG correspondant à la ténacité à la rupture et au module de stockage de la lamina propria. La composition de gel à 30 %

a finalement été choisie en raison de son profil de dispersion plus réaliste et de sa porosité accrue. Les résultats ont montré que la géométrie de l'aiguille et la structure de l'échafaudage influençaient la déformation et les forces de friction associées à l'insertion de l'aiguille. La force maximale globale générée par l'injection est supérieure à celle produite par l'insertion de l'aiguille. Il a été constaté que la force moyenne et la durée de l'injection sans aiguille étaient respectivement 18x plus grandes et 20x plus petites que les memes valeurs pour l'injection avec aiguille. L'injection avec aiguille se caractérise par des périodes individuelles d'insertion, d'injection et de retrait de l'aiguille, tandis que l'injection sans aiguille se caractérise par une vibration de grande amplitude qui décroît de façon exponentielle. Après l'impact initial, les résultats morphologiques ont montré que la profondeur et la largeur moyennes de la NFLJI étaient 1,9 fois et 1,7 fois supérieures à celles de l'injection à l'aiguille. Le bolus injecté par l'aiguille est étendu radialement à partir de la pointe de l'aiguille, tandis que le bolus provenant de l'injection de NFLJI est étendu verticalement le long d'une longue tige.

La variation des paramètres expérimentaux a entraîné des changements dans la force, la durée, la largeur et la profondeur associées à chaque technique d'injection. Les résultats a ce jour indique que la viabilité cellulaire de l'injection à l'aiguille est 1,1 fois supérieure à celle de l'injection sans aiguille. L'injection sans aiguille produit un vide matériel significativement plus important que l'injection avec aiguille, ce qui indique que la force d'injection est proportionnelle à la lésion et à la déformation des tissus. L'injection à l'aiguille s'est avérée être une technique mieux adaptée l'administration de médicaments dans les cordes vocales. L'augmentation de la durée et la réduction de la force de l'injection à l'aiguille ont permis une injection superficielle fiable avec un minimum de lésions tissulaires. Bien que la diminution de la durée et l'augmentation de la

profondeur de la NFLJI aient probablement contribué à la réduction de la douleur et des saignements occasionnels observés avec cette technique, la force et la largeur d'injection de la NFLJI devraient être réduites pour sa mise en œuvre clinique.

IV ACKNOWLEDGEMENTS

I would like to begin by acknowledging Prof. Mongeau for his guidance, mentorship, and support. His expertise and knowledge within the mechanical and biomedical engineering field were instrumental to my project. I would like to extend an additional acknowledgement to Anna Henley and Zixin He for their assistance throughout the entire project. Anna's thesis work served as the basis for which my project was built upon. In addition, Anna supported the project by offering unconditional help and expertise along the way. Zixin supported the project by designing the test apparatus and assisting in the collection of data. Next, I would like to thank the Mongeau lab group. The following individuals provided training and offered support when needed: Kaustuv Basu, Alicia Reyes Valenzuela, Sara Nejati, Swen Groen, Xuan Li, and Zhen Yang. I would like to also thank the Advanced Bioimaging Facility and the Facility for Electron Microscopy Research.

Outside of the Mongeau lab group, I would like to acknowledge the following groups for their financial support: Medical International Technologies (MIT Canada), the Natural Sciences and Engineering Research Council of Canada (NSERC), the BBME department. I would like to specifically thank Maurice Menassa of MIT Canada for his guidance throughout the project.

Finally, I would like to extend my utmost love, appreciation, and gratitude to my parents. Thank you for your unwavering support and encouragement. You believed in me at my lowest points and celebrated with me at my highest.

V CONTRIBUTION OF AUTHORS

The study of needle-free injectors within the Mongeau lab was initiated by students Anna Henley, Qiman Gao, and Zixin He. The student's previous work looked to investigate the use of needle-free injectors for dental anesthesia, as well as to characterize the dynamic response in a tissue-mimicking phantom. Although the current project has changed in scope, aspects of the author's work have been adapted to it. The apparatus, described in section 3.1, was designed by Anna Henley, Zixin He, Swen Groen, and Rani Taher. In addition, the group's work was used as a point of reference in which current experimental parameters and hypotheses were based upon. In terms of the current thesis, the following was accomplished with the help of Zixin He: modification of the test apparatus, writing of the Simulink code, and collection of preliminary force-time data. The procedure for fabricating the PPG gel was designed by Sarah Nejati. The procedure for cell culture was designed by Sarah Nejati and Alicia Reyes Valenzuela.

VI LIST OF FIGURES

VII LIST OF TABLES

VIII LIST OF ABBREVIATIONS

NFLJI Needle-free Liquid Jet Injection

PPG PEG-PEGDA-GelMA

2D Two dimensional

3D Three dimensional

GelMA Gelatin-methacryloyl

HVFF Human vocal fold fibroblast

LP Lamina propria

PBS Phosphate-buffered saline

1 INTRODUCTION

The vocal folds are a tissue structure in the larynx responsible for regulating airflow and phonation [1]. Consisting of three layers, the lamina propria is the primary structure responsible for transmitting the acoustics vibrations experienced as voice. Voice disorders may involve cellular or mechanical changes within the lamina propria, disrupting the manner in which it responds to glottal flow. Voice disorders may be treated by introducing new materials into the tissue. These materials improve sound wave propagation by bulking the diseased tissue such that desirable phonation characteristics are recovered. Since these materials are usually delivered by needle, there exists a potential to apply NFLJI for vocal fold injection. Needle-free injectors are drug delivery systems that deliver materials through the generation of a high velocity fluid stream. The main advantage of needle-free injection is reduced pain and avoidance behavior for patients with needle phobia [2, 3]. Today, substances commonly injected with NFLJI technology include insulin, human growth hormone, Botox, anesthetic, and vaccines [4]. However, needles still remain a more popular method of drug delivery, largely due to a lack of understanding of NFLJI behaviour. Although some studies have investigated the dispersion pattern of needle-free delivered substances, very few have looked into the dynamic or cellular response experienced post-injection. In addition, previous studies employing non-porous hydrogels have failed to replicate the structure of native vocal fold tissue. Those conducted in-vivo have reported conflicting efficacy, pain, and patient compliance results. The lack of biological accuracy and consistency among current NFLJI research highlights the need to better understand needle-free injection to inform eventual clinical adaptation.

The rationale of the research was to contribute to the medical community's understanding of needle and needle-free injection. Three research objectives were formulated. A hydrogel scaffold

replicating vocal fold tissue was to be engineered. The dynamic and morphological response within the phantom for each injection was studied. The cellular response for each technique was determined in terms of cell viability. Results provide insights on the relative ability of a needle and needle-free injector to deliver vocal fold injections.

1. 1 Research Objectives

1. 1.1 Hydrogel Scaffold Design

The first aim of the study was to design a phantom that could be used as a platform for in-vitro injection. A new phantom was needed, as previous materials used in NFLJI studies lacked either the porous or mechanical structure required to accurately replicate injection into human lamina propria. PEG-PEGDA-GelMA (PPG) was selected as a candidate material due to its porosity, biocompatibility, mechanical tunability, transparency, and manufacturability. The PPG was made with three different concentrations of PEGDA: 10%, 20%, and 30%. The PEGDA concentration was varied to tune the gel's porosity, and its bulk mechanical properties. The storage modulus, elastic modulus, fracture toughness, porosity, and dispersion profile of all gel compositions were measured and compared to those of native vocal fold tissue. The composition most closely matching native vocal fold tissue was selected for the needle and NFLJI injections.

1. 1.2 Dynamic Response and Bolus Morphology

The second aim of the study involved characterizing the dynamic and morphological response of both injection techniques. The dynamic response was recorded in terms of injection force and duration. The morphological response was characterized in terms of the injected material's vertical depth and horizontal spread. The results provided insight on device efficacy, safety, pain, and viability. Needle and NFLJI parameters were varied to provide complementary insight on the

injection outcomes experienced at different clinically relevant operating conditions. In order to accomplish this objective, the PPG composition selected in Aim 1 was used. The varied needle injection parameters included insertion rate, injection rate, liquid volume, and needle gauge. Needle-free injection varied parameters included to liquid volume and driving pressure

1. 1.3 Biological Response Analysis of Needle Injection and NFLJI

The third aim of the study was to characterize the biological response for both injection techniques at the cellular level. Cell viability was selected to quantify the cellular response, as well as the invasiveness and disruption, brought about by each injection type. Attempts were made to relate cell viability and the results of Aim 2. The PPG composition selected in Aim 1 was first seeded with human vocal fold fibroblasts (HVFFs). The scaffold was then injected and stained with a live-dead assay.

2 LITERATURE REVIEW

2. 1 VOCAL FOLD TISSUE

2. 1.1 Physiology

The vocal folds are a pair of tissue membranes located in the larynx. The folds consist of 3 layers: epithelium, lamina propria, and muscle [5]. The lamina propria (LP) is located below the epithelium and above the muscle layer [6]. The LP can be further categorized into superficial, intermediate, and deep layers. Together, the epithelium and superficial LP form a pliable mucosal layer termed the vocal fold "cover". Below the cover, the deep and intermediate lamina propria form the vocal ligament or "body". The LP layers become more rigid with depth due to an increase in elastin and collagen fibers [7-10]. In addition, the deeper LP layers have a higher concentration of interstitial proteins and a reduced concentration of extracellular matrix proteins [6]. The most prominent cells within the vocal folds are fibroblasts. Macrophages and myofibrils are also found in the superficial LP to target wound healing and injury [6].

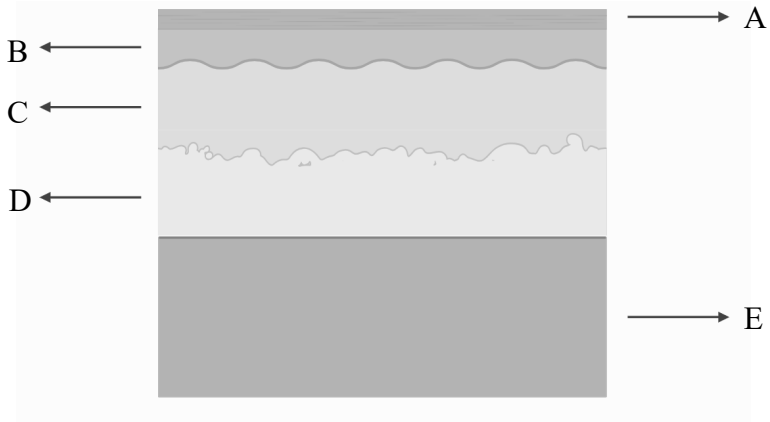

Figure 1: Cross section of vocal fold tissue depicting the epithelium (A), superficial lamina propria (B), intermediate lamina propria (C), deep lamina propria (D), and muscle layers (E). Adapted from "Skin epithelium", by BioRender.com (2024). Retrieved from https://app.biorender.com/biorender-templates.&apos

2. 1.2 Phonation and Vocal Fold Disorders

The main roles of the vocal folds are to prevent food from entering the airways and to regulate airflow for respiration and phonation [1]. Phonation is initiated when air is expelled from the lungs and into the larynx. Airflow induces self-oscillation of the vocal folds, causing them to fluctuate between an open and closed states. During this motion, a self-sustaining acoustic wave is produced within the cover layer [11, 12]. The acoustic wave is then transmitted from the larynx to the oral cavity where it is released as sound [12]. Phonation characteristics depend on the tissue's mechanical properties and the manner in which the cover responds to respiratory flow [1, 6, 13]. The mechanical properties of the vocal fold cover change with age and overall health. In terms of health, vocal fold disorders often cause the tissue to stiffen or change superficially in mass and structure. The tissue changes modify sound wave propagation and the resulting phonation characteristics [14]. Vocal fold disorders are detected in terms of reduced volume, stamina, range, or vocal ability. The disorders result from voice overuse, smoke inhalation, acid reflux, alcohol abuse, air pollution, allergies, inflammation, pathogens, cancer, surgical intervention, and aging [15]. Voice disorders can be treated by introducing new materials to the tissue. This technique is used when voice therapy, a common treatment method, has been ineffective. The injected materials address phonatory defects by filling the tissue to re-establish healthy vibrational characteristics in the presence of defects, masses, and scarring [16-18]. Collagen-based materials are most commonly used for this application although alternatives exist in the form of hyaluronic acid, autologous fat, and acellular dermal matrices, among others [6, 14, 19]. Commercially available products include Zyplast, Gelfoam, Surgifoam, Cymetra, and Cosmoplast/Cosmoderm [20]. Injections are most commonly delivered to a depth of 5 mm by needle [10]. Needle gauges of 18G

to 27G are most popular. Needle insertion and material injection are performed as slowly as possible to avoid penetration of the injection into the surrounding tissue and deeper muscle layers.

2. 1.3 Mechanical Properties

Vocal fold mechanical properties are intrinsic to tissue functionality and serve as benchmarks for evaluating overall tissue health [15, 21]. The storage modulus is often used for characterizing the vocal folds. This parameter is measured through the application of a shear stress, replicating in-vivo vibrational forces [22, 23], and defines the tissue's ability to store energy elastically [21]. A summary of published storage modulus values for human vocal fold LP is shown in Table 1. Results are reported in terms of investigator and the method they used to exert a shear force on the tissue.

Table 1: Storage modulus of human vocal fold cover as reported in the literature per author and evaluation method.

Author	Method of Evaluation	Value (Pa)
Teller et al [11]	Torsional Wave Experiment Apparatus (TWE)	617 - 843
Goodyer et al [19, 24, 25]	Parallel Plate	1008 - 1273
	Indentometer	1000 - 1332
	Linear Skin Rheometer (LSR)	814 - 1796
Miri et al [1]		380 - 1300
Chhetri et al. [25]		1076-1307

The elastic modulus is measured through the application of a contractile or tensile stress, replicating the force exerted on the tissue by the deep muscles [1]. It defines the tissue's ability to

resist deformation [21]. A summary of published elastic modulus findings for human vocal fold LP is shown in Table 2.

Table 2: Elastic modulus of human vocal fold cover as reported in the literature per author and evaluation method.

Author	Method of Evaluation	Value (kPa)
Chhetri et al [23]	Indentation	2 - 7.5
Chan et al.	Low Strain Uniaxial Traction Test	11.611 -15.35
Zhang et al [26]		0.6 - 3.73
Tran et al [27] [27]	Linear Skin Rheometer (LSR)	0.11 - 4.41

Fracture toughness quantifies a material's ability to resist the generation of a crack [1, 28]. As a result, this property is of specific interest when studying needle insertion. Measurements are made by subjecting a tissue sample to two consecutive fractures. The material toughness can then be determined by quantifying the difference in energy between the two insertions. Although this technique is commonly used, fracture toughness is sensitive to the cutting tool's geometry and kinematics, leading to great variation in reported values. Only one study has characterized the fracture toughness of human vocal fold tissue [28]. Other studies have measured the fracture toughness of similar tissue types and various hydrogel materials. A summary of published fracture toughness findings for various materials is shown in Table 3.

Table 3: Fracture toughness values as reported in the literature per author and evaluation method.

Author	Method of Evaluation	Material	Value (J/m^2)
Amir et al. [1]	Razor Blade Cutting	Porcine Vocal Fold LP	164.9 - 468.2
Taheri et al. [29] [29]	Notched Sample Tensile Testing	Single Network Hydrogel	1
		Double Network Hydrogel	39
Azar et al. [30]	Needle Insertion	Porcine Liver	30.75 - 185.6
		Oral Mucosa	28.37 – 35.36
Henley et al.		Gelatin Gel	1.48 - 5.32
		pHEMA Hydrogel	17.26 – 21.14

2. 2 NEEDLE INJECTION

Needle injection is one of the most common procedures in modern healthcare. Needles deliver fluid below the surface of soft tissue by way of a hollow metal tube [31]. The first hypodermic needle was invented in 1844 and paired to a syringe in 1853 to inject morphine [32]. The basic needle-syringe system has remained unchanged since then. The syringe consists of a fluid chamber and a plunger. When pressure is applied to the syringe, the plunger transfers a force onto the liquid in the fluid chamber, pushing it out of the needle tip.

The behaviour of needle insertion can be divided into the following four phases: deformation, penetration, relaxation, and needle withdrawal [30]. Deformation occurs when the needle first meets the tissue. The needle deforms and eventually punctures the tissue once it overcomes the necessary energy threshold. Once punctured, the needle penetrates the tissue until it reaches its targeted depth. Tissue relaxation occurs at the maximum depth once the needle becomes stationary.

The relaxation associated to the tissue's viscoelastic properties, occurs until needle extraction begins. As the needle withdraws from the tissue, it is subjected to frictional forces and a release of energy. Although work has been done to characterize needle insertion, very little progress has been made towards better understanding needle injection and the interaction between injected fluid and the surrounding tissue. It has however been reported that the subcutaneous injection bolus expands from the needle's tip and has a spherical shape in the tissue [33]. The characteristics of the needle impact the resulting forces. This includes the needle tip geometry and diameter, as well as the rate at which the needle and the fluid move within the tissue.

2. 3 NEEDLE-FREE INJECTION

2. 3. 1 History and Current Use

Needle-free injectors have been suggested as an alternative injection technique [34, 35]. Needle-free liquid jet injection (NFLJI) was conceptualized in the 1930s and commercially introduced in the 1940s to deliver insulin and to treat orthopaedic conditions [3, 36-38]. The ability to deliver consecutive doses with the same device made NFLJI extremely attractive, leading to its future development for large scale vaccination campaigns among other applications [36]. Today, NFLJI is used to administer the following substances subcutaneously, intradermally, and intramuscularly: insulin, human growth hormone, vaccines, Botox, and anesthetic [4]. The main advantage of needle-free injection is reduced avoidance behavior for patients with needle phobia. Needle phobia, or fear induced by the presence of a needle, is an inherited or acquired condition that impacts 33-63% of children and 14-38% of adults [2, 3]. Needle-free injection increases compliance among needle phobic patients and reduces the likeliness that they avoid necessary medical treatments. In addition, NFLJI reduces the risk of cross infection and needle stick injuries. Reduced infection benefits both the developing and developed world, as unsafe needle practices

are responsible for up to 40% of HBV and HCV cases in developing countries [35, 39]. Additional benefits of NFLJI include reproducibility, reusability, feasible self-administration, compatibility with dosages designed for needles, and improved ease of use for individuals with impaired motor skills [38, 40, 41].

However, NFLJI has failed to replace conventional needles entirely [34]. This is largely due to a limited understanding of the associated tissue response. Needle-free injection has been most commonly evaluated qualitatively through clinical trials. Studies have reported conflicting results in terms of device efficacy, safety, pain, and patient compliance that vary with the injection application and study group demographics [34, 36, 38, 42]. The clinical results of both needle and needle-free injection are comparatively discussed in further detail in section 2.1.4. In addition to clinical research, in-vitro studies have been conducted to determine the dispersion of NFLJI delivered substances [4, 43]. However, these studies relied on non-porous hydrogels and cadaver tissue, failing to recreate the non-homogenous structure and fluid dynamics experienced in-vivo [38]. These studies failed to explore the dynamic or cellular response during and post-penetration. The lack of insight regarding needle-free injection in-vivo, paired with a high cost of adaptation and need for continuous maintenance, have therefore served as barriers to their widespread use.

2. 3. 2 Injection Mechanics and Dynamics

Needle-free liquid jet injectors are pneumatically actuated drug delivery devices that produce a high velocity fluid jet. Needle-free injectors are composed of the following components: a pressure generator, piston, injection chamber, and a nozzle [41]. The majority of modern devices use pressurized gas to generate force. The pressurized gas allows for precise control over injection characteristics, such as penetration depth and liquid volume, and increases adaptability towards

various tissue types and clinical applications [35, 36, 44]. Once in the device, the pressurized gas accelerates the power piston forward until it reaches the injection piston and fluid-filled injection chamber, causing the liquid within to be ejected through the nozzle.

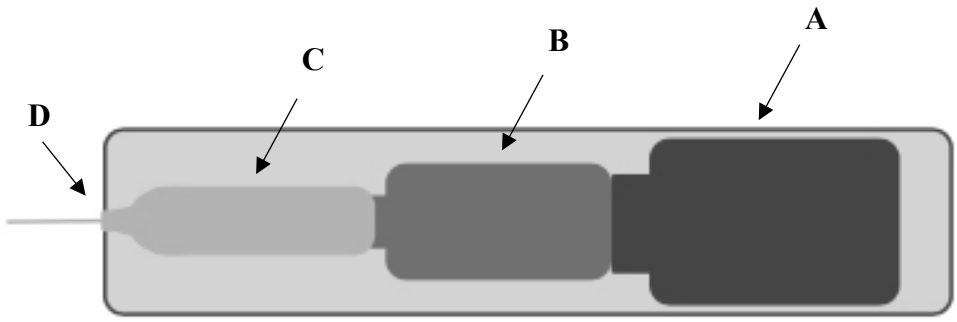

Figure 2: A schematic of the needle-free injector's internal system. The power piston [A] collides leftwards with the injection piston [B]. The fluid piston than collides with the liquid held in the injection chamber [C], ejecting the liquid out of the nozzle [D]. Created with BioRender.com.

The action of NFLJI delivered fluid can be divided into two phases. The first phase entails tissue puncture by fracture and erosion [38]. Fracture is caused by forming a hole in the tissue when the liquid's stagnation pressure overcomes the tissue's elastic forces [4, 45]. The second phase begins as liquid accumulates and expands. Several studies have reported that liquid expands to form a cylindrical bolus when injected into porous tissue [44, 46-48]. Liquid instead extends through "penny shaped cracks" in non-porous materials [49]. As a result, NFLJI can be evaluated in terms of the dispersion pattern obtained during liquid expansion [46]. The pattern, believing to provide insight on fluid absorption and injection pain, is dependent on the tissue's mechanical properties and the jet's injection profile [46, 50]. The device's fluid pressure, fluid volume, nozzle diameter, and stand-off distance greatly affect the jet's profile [46]. An increase in fluid velocity, nozzle

diameter, and liquid volume have been linked to a decrease in stagnation pressure and an increase in penetration depth [4, 36, 46, 50, 51].

2. 4 Comparison Between Needle and Needle-free Injection

Needle and NFLJI comparative studies have been compared in terms of relative pain and efficacy [34]. Approximately 76% of study participants, specifically children, prefer needle-free to needle injection due to reduced pain [38, 42]. Study participants have compared the sensation of NFLJI to a "short pinch" and needle injection to a "prolonged sensation" [52]. In terms of efficacy, needle-free injectors have administered vaccines, gene therapies, growth hormones, insulin, steroids, and antibiotics at an effectiveness equivalent or greater than that of a needle [44, 53]. Specifically, vaccines delivered by NFLJI were found more widely dispersed throughout the tissue, increasing the degree of contact with immune cells, and leading to improved delivery of the following vaccines: typhoid, influenza, polio, meningitis, yellow fever, hepatitis A, measles, smallpox, and cholera vaccines [34, 36, 38]. Similarly, needle-free delivered gene therapies, growth hormones, and insulin were taken up more rapidly when delivered by NFLJI [34, 36, 38]. However, promising NFLJI results have been met clinically by higher rates of unpredictable and occasional pain, bleeding, and bruising than needle injection [38]. In addition, patients have expressed greater difficulty with NFLJI self-administration compared to that of a needle. Improper administration leads to "wet" injections where a significant percentage of the fluid fails to penetrate the tissue [38]. Additional studies have been conducted in an attempt to explain conflicting patient experiences. The most notable study compared injection dynamics between needle and needle-free injection using a pHEMA hydrogel phantom. Results determined that the duration and work of injection were significantly decreased and increased with NFLJI [54]. The study therefore suggested that injection duration might be responsible for the decreased pain experienced with

needle-free injection. However, further investigation is required to explain the unpredictable and occasional pain, bleeding, and bruising of this injection technique.

2. 5 HYDROGEL PHANTOMS

Hydrogel phantoms are tissue-mimicking structures used to develop, validate, and optimize medical techniques [55]. Phantoms have been used to train clinicians performing biopsies, vascular punctures, and CT drainage [56]. Phantoms should reproduce the physical, chemical, and mechanical properties of native tissue, as well as be inexpensive, capable of repeated use, and able to provide physical feedback [57, 58]. Common material choices are water, gelatin, elastomeric rubber, meat, or cadaver tissue [57]. Gelatin has specifically been used to model cysts, nodules, and neck anatomy [56]. Although phantom design for vocal fold tissue has been limited, the following materials have been used to mimic the superficial tissue structure: silicone, cell-seeded agarose, and polyethylene glycol [59-61]. As a result, there exists a need to develop better vocal fold phantoms that represent both the tissue's structural and mechanical complexity [61].

3 METHODOLOGY

3.1 APPARATUS

3. 1.1 Apparatus Design

A custom apparatus was used to record needle and NFLJI force and time data. A schematic diagram of the apparatus is shown in Figure 3. Needle and NFLJI test configurations are shown in Figure 4. The apparatus consisted of a 3D printed hydrogel platform. The platform was installed on top of a strain gauge force transducer (GSO500, Transducer Techniques, USA) and fixed to a

laser table. The transducer signal was fed to a data acquisition system (Model, National Instruments Corp., USA), allowing the force exerted on the hydrogel platform to be recorded and transmitted to Simulink software for analysis. All data was acquired at a sampling rate of 10 000 Hz. The data was exported from Simulink as an excel file to be processed in Matlab (MathWorks Inc,. MA). In order to administer continuous injections in a reproducible manner, the needle and needle-free injector (MIT Canada, Montreal, QC) was secured to a motorized linear traverse (Velmex, USA) above the hydrogel platform. The motorized traverse controlled the device's motion in the y-direction while maintaining a fixed position in the x-direction. In the case of the needle, the traverse controlled the rate and depth at which the needle descended into the gel. The needle extrusion was powered by a syringe pump (New Era Pump Systems Inc., USA) and coupled via T connector (Ticomi, USA). The pump delivered the fluid through the needle at a preprogrammed rate and volume. For the needle-free injector, the traverse controlled the device's position above the hydrogel. Pressurized CO_2 was used to trigger the device and initiate liquid ejection out of a preloaded cartridge. As a result, the driving pressure and the cartridge's liquid volume determined the rate and volume of fluid delivery.

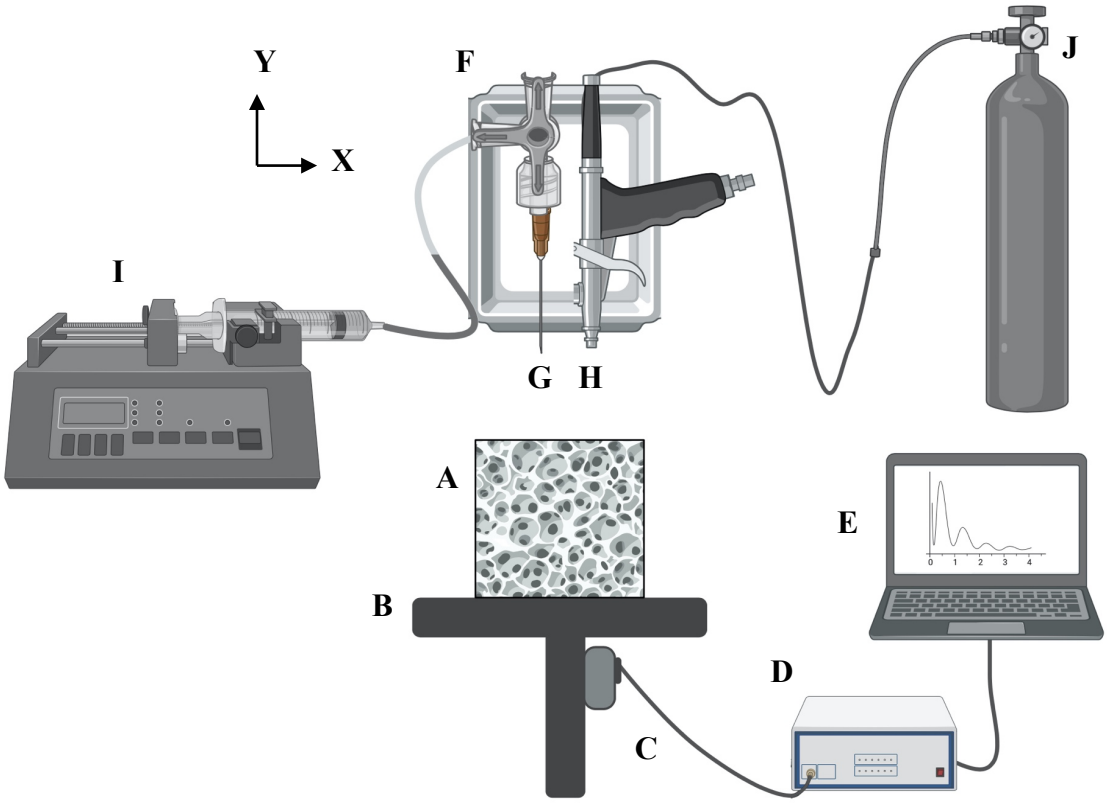

Figure 3: Schematic diagram of the apparatus. A PPG hydrogel [A] is positioned on a 3D printed platform [B]. The platform is installed atop a strain gauge force transducer [C]. The force transducer transmits recorded force data to a computer Simulink program [E] by data acquisition system [D]. The needle [G] and needle-free injector [H] are suspended above the hydrogel by a linear traverse [F]. The needle flow is provided by syringe pump [I]. The needle-free injector is powered by pressurized gas [J]. Note that the diagram components are not shown to scale. Created with BioRender.com

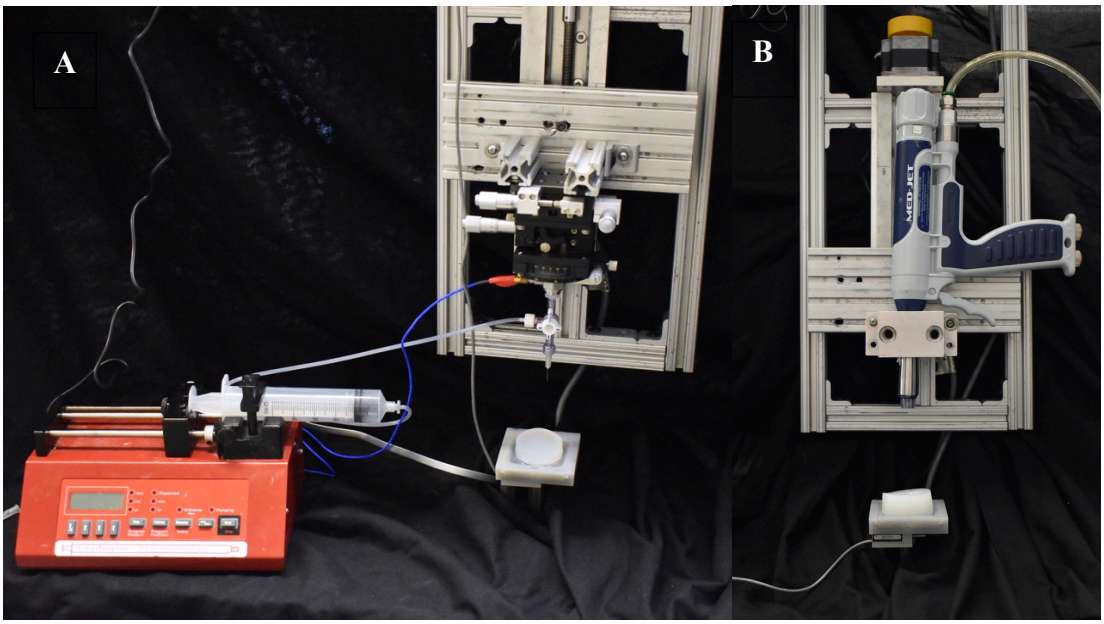

Figure 4:(A) Apparatus configuration for needle injection. (B) Apparatus configuration for needle-free injection.

3. 1.2 Force Gauge Transducer Calibration

The relationship between the transducer's input force and output reading was determined by calibration. Known masses, ranging between 5-100 grams, were incrementally placed on the force gauge transducer. The output voltage was plotted against the force exerted by each respective mass. The force exerted by each mass was calculated by the equation

$$F = mg, \tag{1}$$

where F is the force in N, m is the mass in kg, and g is the force of gravity in N. The data was then imported to Matlab and fit by a linear equation of the form y = mx + b. All future data acquired by the force gauge transducer was subject to the established equation.

3.2 MATERIAL SYNTHESIS

3. 2.1 GelMA

A 10% GelMA solution was synthesized with II bovine gelatin (9000-70-8, Sigma-Aldrich) and methacrylic anyhydride (760-93-0, Sigma-Aldrich). 10 g of gelatin and 12 mL of methacrylic anyhydride were added to 100 mL of DI water. The solution was wrapped in tinfoil to prevent light exposure and magnetically stirred on a 60 °C plate for 3 hours. After 3 hours, 400 mL of DI water was added to the solution. The mixture was stirred for an additional hour and then placed in dialysis tubes. The tubes were suspended in ~400 mL of DI water and kept in a 37°C incubator for 3 days. The water was changed daily to remove extracted impurities. Once complete, the solution was removed from the dialysis tubes and distributed into 50 mL conical tubes. The tubes were frozen at -80°C for 12 hours before being placed into a freeze dryer. The GelMA remained in the -84°C freeze drier for 4 days before reaching its final state.

3. 2.2 LAP (Lithium phenyl-2,4,6-trimethylbenzoylphosphinate) solution

A 3% LAP solution was produced by adding 0.3 g of LAP (85073-19-4, Sigma-Aldrich) to 10 mL of DI water. The solution was wrapped in tinfoil to prevent light exposure and stirred at room temperature conditions (21°C) for 24 hours until completely dissolved.

3. 2.3 PEG-PEGDA-GelMA (PPG)

PPG synthesis began by preparing an 8% PEGDA and 2% GelMA solution. 0.8 g of PEGDA (INDOFINE, USA) and 0.2 g of GelMA were added to 10 mL of DI water. Next, 1 g, 2 g, or 3 g of PEG (25322-68-3, Sigma-Aldrich) were added to the solution to achieve compositions of 10%, 20%, and 30% PEG. The solution was stirred on a 60 °C plate for 2 hours. After stirring,

1mL of LAP solution was added and the mixture was sterilized with 0.45 um filters (SLHV033NS, Sigma Aldrich). The sterilized solution was then poured into molds and crosslinked with UV light (NailStar Professional 36W UV Nail Dryer Nail Lamp, NS-01-US&CA, batch 20032610). The duration of UV exposure was dependant on the dimensions of the gel. Hydrogels molded with a thickness of 1 mm were exposed to 30 s of UV light. Hydrogels molded with a thickness of 20 mm or 40 mm were exposed to 1 and 2 min of UV light. After curing, the PPG gels were washed to allow for pore formation. The gels were suspended in PBS (10010023, ThermoFisher) and placed in a 37°C incubator. Hydrogels molded with a thickness of 1 mm were washed for 2 days. Hydrogels molded with a thickness of 20 mm or 40 mm were washed for 5 and 7 days. The PPG gels were fully synthesized once washing was complete.

3. 2.4 Methylene Blue Saline Solution

A 0.9% methylene blue saline solution was produced by adding 0.45 g of methylene blue (PHR3838, Sigma Aldrich) to 50 mL of saline (6240, Nurse Assist Inc.) The solution was vortexed at room temperature conditions (21°C) for 1 minute until completely mixed.

3. 2.5 Cell Viability Assay

A commercially available cell viability kit (L3224, ThermoFisher) was prepared by dissolving 20 uL of 2mM EthD-1 and 5 uL of 4mM calcein AM in 10 mL of tissue culture grade D-PBS (14040117, ThermoFisher). The solution was vortexed at room temperature conditions (21°C) for 1 hour until completely dissolved.

3.3 HYDROGEL SCAFFOLD CHARACTERIZATION

3. 3.1 Storage Modulus

The storage modulus was recorded using a parallel plate torsional rheometer (Discovery II, TA Instrument, USA). PPG samples consisting of 10%, 20%, and 30% PEGDA were synthesized and cast in custom circular molds, as described in section 3.2.3. The molds had a diameter of 10 mm and a height of 1 mm. After washing, the samples were positioned on the rheometer base plate below a 10 mm diameter upper plate piece. A time sweep was conducted for 120 seconds at a strain of 0.1%, frequency of 1 Hz, and temperature of 37°C. A low frequency of 1 Hz was selected for this study as exposing soft tissue to frequencies larger than 10-15 Hz can lead to significant errors [7, 62]. The storage modulus was directly extracted from the recorded data using TRIOS software (TA Instrument, DE).

3. 3.2 Elastic Modulus

The elastic modulus was recorded using an InstronTM machine (Model 5965, 10 N load cell). PPG samples consisting of 10%, 20%, and 30% PEGDA were synthesized in custom rectangular molds, as per the protocol in section 3.2.3. The molds had a length of 80 mm, width of 35 mm, and thickness of 1 mm. After washing, acrylic sheets were glued to either end of the hydrogel. The sheets were then clamped to the Instron machine and used to vertically fix the material. During testing, the clamps pulled the acrylic sheets in opposite directions, indirectly imposing a tensile force on the loaded gel. A diagram of the testing configuration is displayed in Figure 5. Tensile stretching was performed with a 10N load cell at a rate of 2% until material yield. All data was recorded and analyzed with Bluehill Universal software (INSTRON, USA).

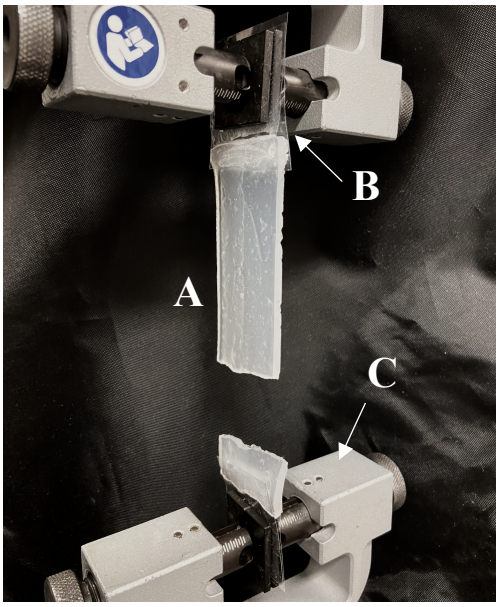

Figure 5: Diagram of hydrogel tensile testing configuration depicting the hydrogel [A], acrylic sheets used to load the sample [B], and the clamps [C].

The elastic modulus was calculated by transforming the recorded force and displacement values into stress and strain values. Stress was calculated by dividing the recorded force by the cross-sectional area of the gel samples, as follows

$$\sigma = \frac{F_{tensile}}{A_{cross\ section}}, \tag{2}$$

where σ is the resulting stress in Pa, $F_{tenstile}$ is the tensile force applied to the sample in N, and $A_{cross\ section}$ is the cross-sectional area of the sample in m^2. Strain was determined by dividing the length of the gel upon yield by its original length, as follows

$$\varepsilon = \frac{l_{new} - l_{0original}}{l_{0original}}, \tag{3}$$

where ε is the resulting material strain, l_{new} is the sample length immediately before yield in m, and $l_{original}$ is the original length of the sample in m.

$$E = \frac{\sigma}{\varepsilon}, \tag{4}$$

where E is the elastic modulus in Pa, σ is the material's stress in Pa, and ε is the material's strain.

3. 3.3 Fracture Toughness

Fracture toughness was determined by a procedure adapted from Azar et al [30]. PPG samples consisting of 10%, 20%, and 30% PEGDA were synthesized in circular molds, as described in section 3.2.3. The molds had a diameter of 35 mm and depth of 20 mm. After washing, the samples were placed on the apparatus's hydrogel platform. The gels were then subject to two identical and consecutive needle insertions. The first needle punctured the material upon entry, exerting both fracture and frictional dynamics. The second insertion penetrated through the previously established hole, exerting only friction forces. The difference in work between the two insertions was used to determine the material's fracture toughness.

Work was calculated by integrating the force of each insertion with respect to needle depth, as follows

$$W = \int_{x_0}^{x_{final}} F\, dx, \tag{5}$$

where W represented the work of each insertion in J, F represented the force of insertion in N, dx the change in needle displacement in m, x_0 the needle's zero displacement position in m, and x_{max}

the needle's maximum displacement position in m. The insertion force was recorded by experimental apparatus. A syringe-pump driven flat tip needle was used for both the primary and secondary insertion. The needle reached a depth of 20 mm into the gel and was kept for 1 second before being removed. The data acquired during insertion was exported to Matlab for plotting. The difference in work between the two insertions was divided by the product of the needle's diameter and maximum displacement position to calculate fracture toughness, as follows

$$F_T = \frac{W_{2nd\ insertion} - W_{1st\ insertion}}{\pi D_{needle} x_{final}}, \quad (6)$$

where F_T represented the fracture toughness in J/m^2, $W_{2nd\ insertion}$ - $W_{1st\ insertion}$ the difference in work between the two insertions in J, and D_{needle} the needle's diameter in m. Fracture toughness was calculated at various insertion speeds and needle gauges to investigate the effect of needle geometry and kinematics. Insertions speeds of 5mm/s, 10mm/s, and 20mm/s and needle gauges of 18G, 21G, and 25G were explored.

3. 3.4 Porosity

The 10% and 30% PPG hydrogel samples were synthesized in circular molds, as described in section 3.2.3. The molds had a diameter of 10 mm and height of 1 mm. The 20% PPG composition was not imaged as it had been eliminated as a candidate hydrogel given its storage modulus, elastic modulus, and fracture toughness results. The samples were washed and sputter coated with platinum at a thickness of 4nm (Leica Microsystems EM ACE600 High-Resolution Sputter Coater with Room Temperature Stage). The coated samples were then subject to porosity imaging via SEM (FEI Quanta 450 Environmental Scanning Electron Microscope (FE-ESEM)). Images were

taken at magnifications of 5,000x, 10,000x, and 20,000x. Image analysis and the quantification of pore size were performed using Xt Microscope Server software (FEI Quanta, USA).

The 10% and 30% PPG hydrogels were injected to determine the effect of porosity on liquid distribution. Here, the 10% PPG sample represented a minimum porosity structure while the 30% PPG sample represented a maximum porosity structure. The gels were cast in circular molds with a diameter of 35 mm and a depth of 20 mm, as described in section 3.2.3. A syringe-pump driven beveled needle tip was used to inject the PPG hydrogels. The needle was filled with 0.9% methylene blue (PHR3838, Sigma Aldrich) saline solution. The needle punctured the hydrogel and reacched a maximum depth of 5 mm. The needle was kept at this depth for one second before beginning injection. The needle remained stationary for 1 additional second after injection before retraction. The injection was delivered at a rate of 0.9 mL/min, insertion of 5mm/s, volume of 0.1 mL, and with a 25 G needle. The liquid distribution was qualitatively assessed.

3.4 Dynamic Characterization

3. 4.1 Needle Insertion and Injection

Needle dynamics during insertion and injection were comparatively analyzed. The 30% PPG hydrogels were synthesized for needle injection, as per the protocol in section 3.2.3. The gels were cast in circular molds with a diameter of 35 mm and a depth of 20 mm. Needle insertion was administered at a rate of 5 mm/s with a 25G beveled needle tip. The inserted needle reached a maximum depth of 5 mm and was held in this position for 9 seconds before removal. Needle injection was additionally administered at a rate of 5 mm/s with a 25G beveled needle tip. The needle descended 5 mm into the gel and was held at this depth for 1 second before injection began. A 0.1 mL of 0.9% methylene blue saline solution was injected at a rate of 0.9 mL/min.

After injection, the needle remained at this position for 1 additional second before being removed. The data acquired during insertion was exported to Matlab and smoothed with a moving average filter. The force-time histories of insertion and injection were then plotted. The two profiles were compared in terms of their insertion, relaxation and/or injection, and removal segments, as shown in Figure 6. The labelling of each segment was completed with the aid and insight of previous needle insertion studies [30].

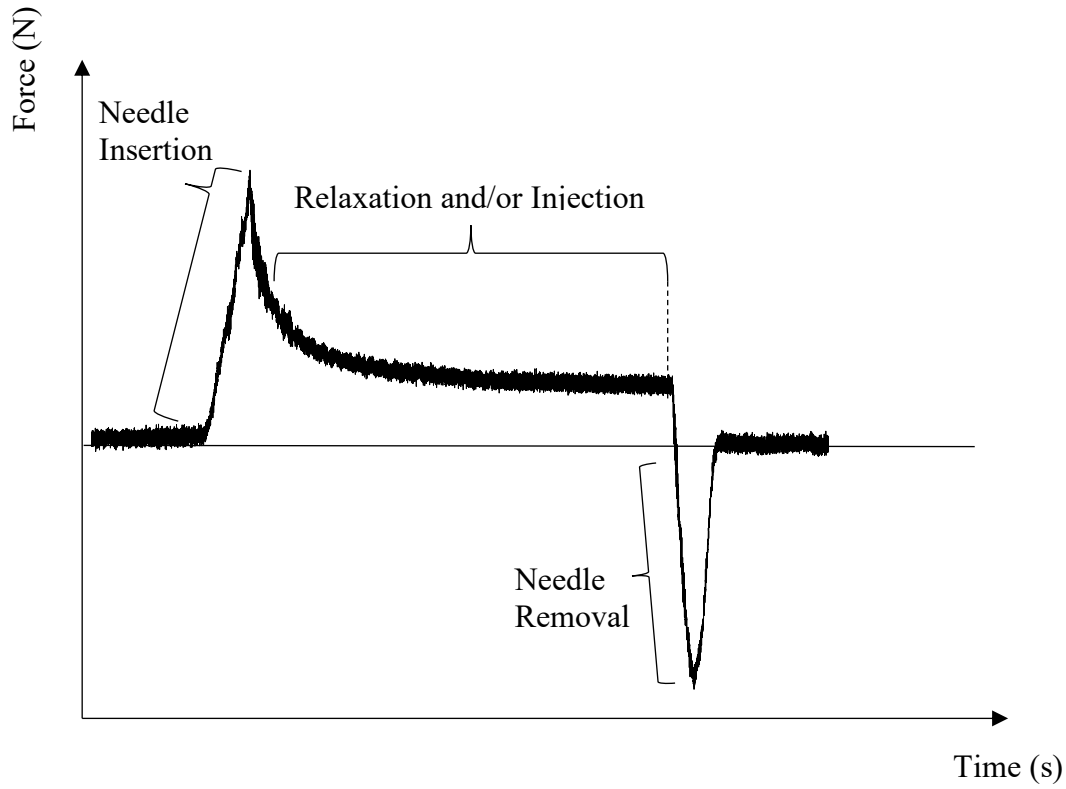

Figure 6: Typical force-time profile for needle insertion and/or injection in which the following three phases are depicted: needle insertion, material relaxation and/or fluid injection, and needle removal.

3. 4.2 Needle Injection

Needle injection dynamics were investigated at various parameters. The 30% PPG hydrogels were synthesized for needle injection, as per the protocol in section 3.2.3. The gels were cast in circular molds with a diameter of 35 mm and a depth of 20 mm. The injection parameters for dynamic characterization were selected based on clinical relevance. Injection rates of 0.9 mL/min, 3.6 mL/min, and 7.2 mL/min alongside insertion rates of 5 mm/s, 10 mm/s, and 20 mm/s were selected. Injections with fluid volumes of 0.05 mL, 0.1 mL, and 0.2 mL and needle gauges of 23G, 25G, and 27G were performed.

The baseline performance conditions consisted of the following: an injection rate of 0.9 mL/min, an insertion rate of 5 mm/s, a volume of 0.1 mL, and a needle gauge of 25G. A single parameter was varied during each injection while the remaining baseline conditions were kept constant. The needle reached and was held at a depth of 5 mm for 1 second before injection of 0.9% methylene blue saline solution began. After injection, the needle remained in this position for 1 second before being removed. Data was acquired at a sampling rate of 10, 000 Hz, filtered, and plotted on Matlab. The filter smoothed the data with a gaussian-weighted moving average filter over a 200-element sliding window. The needle insertion force (F_I), maximum injection force ($F_X\,max$), minimum injection force ($F_X min$), and needle removal force (F_R) were visually extracted from each plot. The overall injection force, encompassing both maximum and minimum values, was represented by F_X. The total duration time (T_T), needle insertion duration (T_I), injection duration (T_X), and needle removal duration (T_R) were visually obtained from each plot. The plot segments representing each force and time value are displayed in Figure 7. The stagnation pressure, shown as

(7)

$$P_S = \frac{1}{2}\rho\left(\frac{Q_{inj}}{SA_{needle}}\right)^2\left(SA_{gel}\right),$$

and the stagnation force, expressed by the following

$$F_S = \frac{P_S}{SA_{gel}}, \tag{8}$$

were calculated as each injection rate to explore the connection between the liquid's velocity and the resulting force. Here, P_s is the stagnation pressure in Pa, ρ is the fluid's density in kg/m^3, Q_{ing} is the liquid injection rate in m^3/s, SA_{needle} is the surface area of the needle's inner cavity, SA_{gel} is the surface area of the gel subject to the needle's fluid delivery in m^2, and F_s is the stagnation force in N.

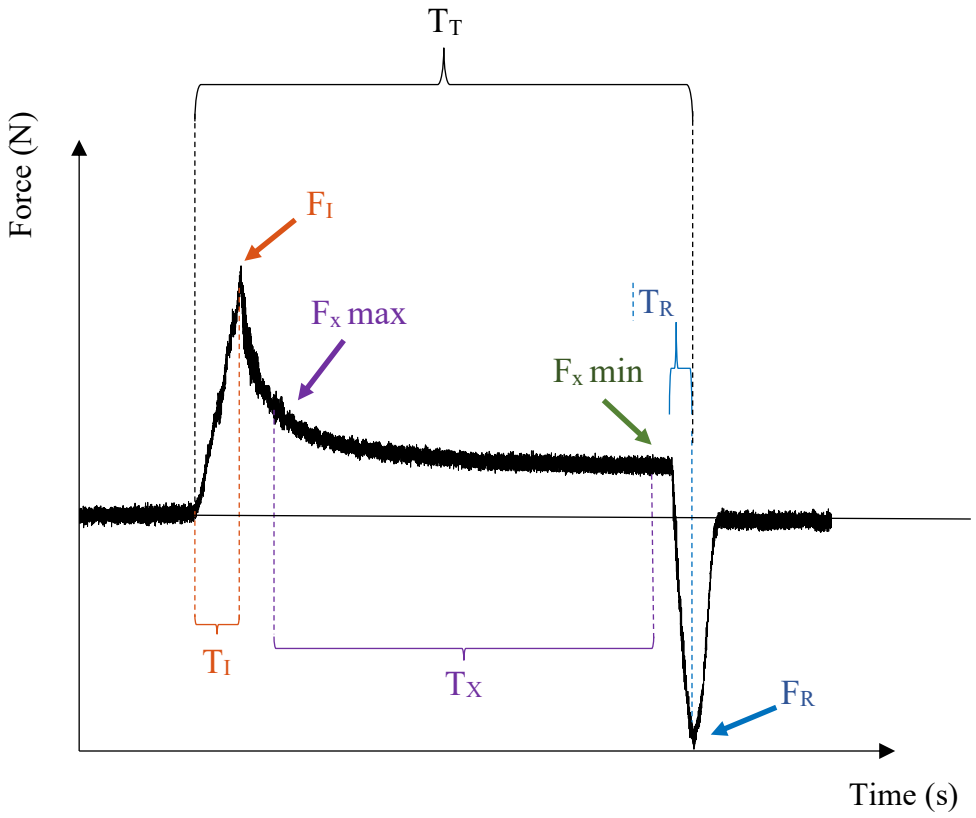

Figure 7: Typical force-time history for needle injection. The needle insertion force (F_I), maximum injection force (F_X max), minimum injection force (F_X min), and needle removal force (F_R) are depicted by the red, purple, green, and blue arrows. The total duration time (T_T), needle insertion duration (T_I), injection duration (T_X), and needle removal duration (T_R) are shown by the black, red, purple, and blue braces.

3. 4.3 Needle-free Injection

The 30% PPG hydrogels were synthesized for needle-free injection, as described in section 3.2.3. The gels were molded as described in section 3.4.2. Deeper hydrogels with a depth of 40 mm were additionally synthesized for injections that penetrated to a depth greater than 20 mm. Injections

were administered at driving pressures of 275 kPa, 448 kPa, and 620 kPa and fluid volumes of 0.05 mL, 0.1 mL, and 0.2 mL.

A pressurized CO_2 tank was used to power the injection. The injector's cartridges were filled with 0.9% methylene blue (PHR3838, Sigma Aldrich) saline solution. To prepare for injection, the injection nozzle was moved above the gel's surface. The traverse remained stationary in this position over the duration of injection. The injection was administered by manually pulling the device's trigger. The baseline performance conditions consisted of a 0.1 mL injection volume and a 448 kPa driving pressure. Either the injection volume or driving pressure varied for each injection while the other condition remained constant. Data was acquired, smoothed, and plotted using Matlab. The maximum force of injection in the positive ($F_{max}+$) and negative (F_{max} -) direction, as well as the total duration of injection (T_T), were derived from each plot. The plot segments representing each force and time value shown in Figure 8.

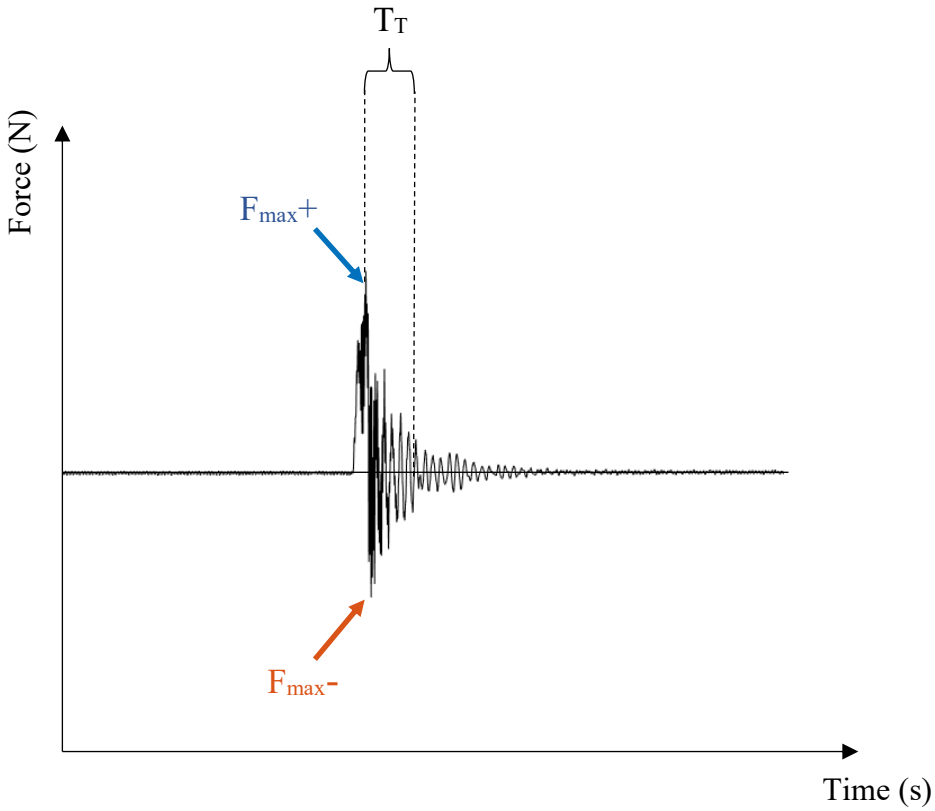

Figure 8: Sample force-time profile for NFLJI in which the extracted force and time values are depicted. The maximum force of injection in the positive (F_{max} +) and negative (F_{min} -) direction are depicted by the blue and red arrows. The total duration time of injection (T_T) is shown.

3.5 Morphological Characterization

The PPG hydrogels from section 3.4.2 and 3.4.3 were vertically sectioned along the injection's midline via a scalpel. Once sectioned, a digital caliper was used to manually measure the injection profile. The profile was measured in terms of the following properties: maximum dispersion depth (D_{max}), minimum dispersion width (W_{min}), maximum dispersion width (W_{max}), depth from gel surface to start of maximum dispersion (D_S), and depth from gel surface to center of maximum dispersion (D_C). The dispersion profile properties, summarized in Figure 9, were selected based on their previous use in characterizing soft tissue injection dynamics [51]. The

sectioned scaffolds were photographed (Canon EOS Rebel T7 18-55mm DC, USA) to visually document the injection profile.

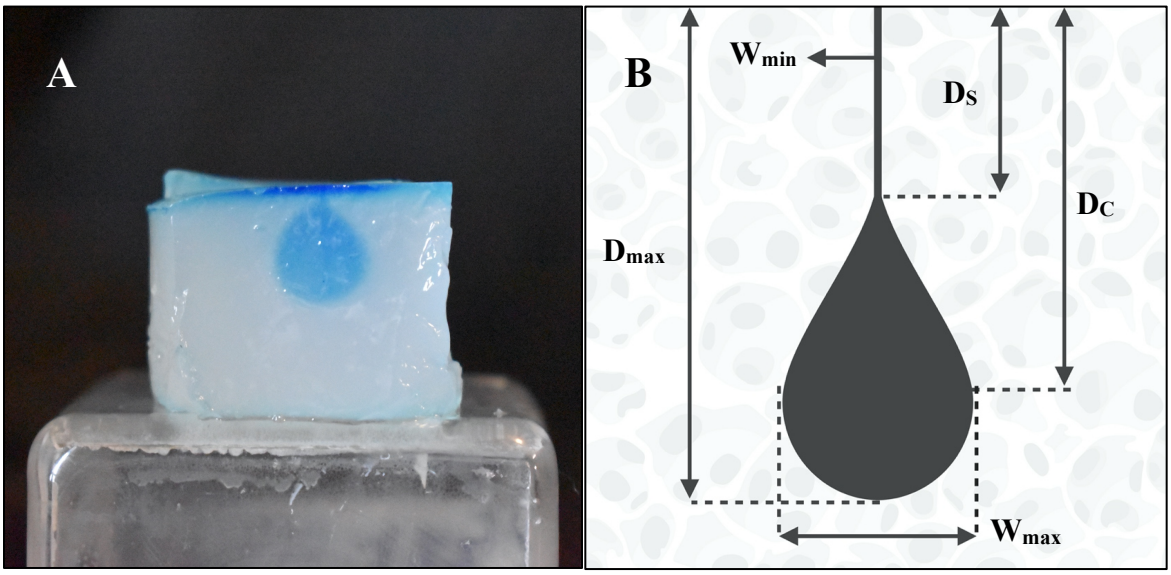

Figure 9: Sample needle injection dispersion profile in 30% PPG hydrogel (A). Schematic needle dispersion profile depicting the maximum dispersion depth (D_{max}), minimum dispersion width (W_{min}), maximum dispersion width (W_{max}), depth from gel surface to start of maximum dispersion (D_S), and depth from gel surface to center of maximum dispersion (D_C) of the injection's profile (B). Adapted from "Macroporous scaffold 3D (small pores)", by BioRender.com (2024). Retrieved from https://app.biorender.com/biorender-templates.&apos

3.6 Biological Characterization

3. 6.1 Hydrogel and Cell Preparation

Immortalized human vocal fold fibroblasts (HVFFs) were cultured in Dulbecco's modified eagle medium (12491015, ThermoFisher) supplemented with 10% fetal bovine serum (F2442-50ML, Sigma Aldrich) and 1% penicillin-streptomycin (15140122, ThermoFisher) in a 37°C incubator

with 5% CO2. The cells were passaged every 2-3 days. Once confluent, cells were dethatched with trypsin (T2600000, Sigma Aldrich) and combined in fresh medium to prepare for seeding.

3. 6.2 Hydrogel Biocompatibility Imaging

The 30% PPG hydrogels were synthesized, as described in section 3.2.3. The gels were cast in circular molds with a diameter of 35 mm and a depth of 1 mm. The hydrogels were seeded with HVFFs at cell density of $5 \bullet 10^5$ cells/mL. This cell density was selected from published growth guidelines that were adjusted to accommodate for the hydrogel's 3D structure [63]. An empty petri dish was seeded with the same cell density to serve as a control. Both the cell seeded hydrogel and control dish were placed in the incubator for 24 hours. After 24 hours, the cell-seeded hydrogel and control dish were stained with 1 mL of cell viability solution such that the entire surface of each was covered. The hydrogel and control dish were then placed in a 37°C incubator with 5% CO_2 for one hour.

Live-dead cell viability was conducted through fluorescent microscopy. Images of the stained hydrogel and control dish were acquired with a Confocal Microscope (LSM 710, Zeiss, Oberkochen, Germany). A 20x objective (20X PLAN APOCHROMAT, NA=0.80) was used to image the cell viability at the direct site of injection. Each image represented a thickness of 60 um. All images were captured and analyzed with Zen software (ZEISS, Germany).

3. 6.3 Needle Injection and NFLJI Imaging

The 30% PPG hydrogels were synthesized, as described in section 3.2.3, in two different molds. The first mold possessed a diameter of 35 mm and a depth of 1 mm. The second mold possessed a diameter of 35 mm and a depth of 20 mm. The 1 mm thick hydrogels were seeded with

HVFFs. The cell suspension was added to the gel such that a cell density of $5 \bullet 10^5$ cells/mL was achieved. An empty petri dish was seeded with the same cell density to serve as a control. The cell seeded hydrogels and petri dish were placed in the incubator for 24 hours. Next, the 1 mm thick cell-seeded hydrogels were removed from the incubator and placed on top of the 20 mm thick acellular scaffolds. The two layers formed a composite hydrogel in which only the most superficial layer contained cells. A schematic summary of the composite hydrogel is displayed in Figure 10. Next, the composite structure was subject to needle or needle-free injection. Needle injection was delivered at an injection rate 0.9 mL/min, an insertion rate of 5 mm/s, a volume of 0.1 mL, and with a 25G beveled tip needle. The needle-free injection was delivered at a driving pressure of 275 kPa and a volume of 0.1 mL. Pure saline was delivered by both the needle and needle-free device. Immediately after injection, the 1 mm thick hydrogel layer was removed from the thicker acellular hydrogel and subject to staining.

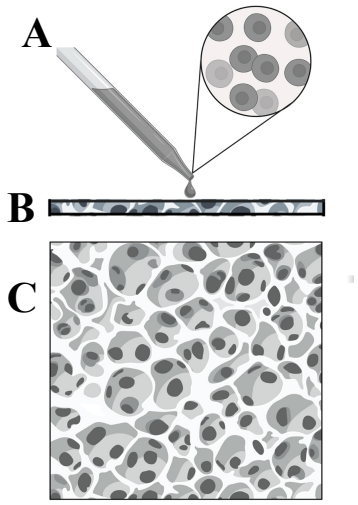

Figure 10: Schematic of the 30% PPG composite hydrogel general assembly depicting the pipette used to deposit the cell suspension [A], the 1 mm thick hydrogel layer [B], and 20 mm thick hydrogel layer [C]. Adapted from "Macroporous scaffold 3D (small pores)", by BioRender.com (2024). Retrieved from https://app.biorender.com/biorender-templates.&apos

The 1 mm thick cell-seeded hydrogel layer and control petri dish were stained with 1 mL of cell viability solution such that the entire injection site was covered. The hydrogels and petri dish were placed in a 37°C incubator with 5% CO_2 for one hour. The live-dead cell viability was imaged via fluorescent microscopy as described in Section 3.6.2. A tiled scan was additionally performed for NFLJI given that the site of injection exceeded the microscope's field of view. The tile scan captured 12 individual images representing an area of 0.25mm^2 each. The stitched images were analyzed with Zen software (ZEISS, Germany).

4 RESULTS

The output voltage vs force exerted by each mass is shown in Table 4. A linear regression of the data yielded the equation $y = 1.127x - 1.118$, as shown in Figure 11. The coefficient of determination had a value of $R^2 = 1$, indicating that the output reading scaled perfectly with the increase in mass. The regression was used to calculate the force exerted on the gauge, y, from the known voltage reading, x.

Table 4: Incremental force gauge reading (V) corresponding to the weight of each mass (N).

Mass (g)	Force (N)	Reading (V)
5	0.05	1.04
20	0.29	1.25
40	0.39	1.34
60	0.59	1.52
80	0.79	1.69
100	0.98	1.86

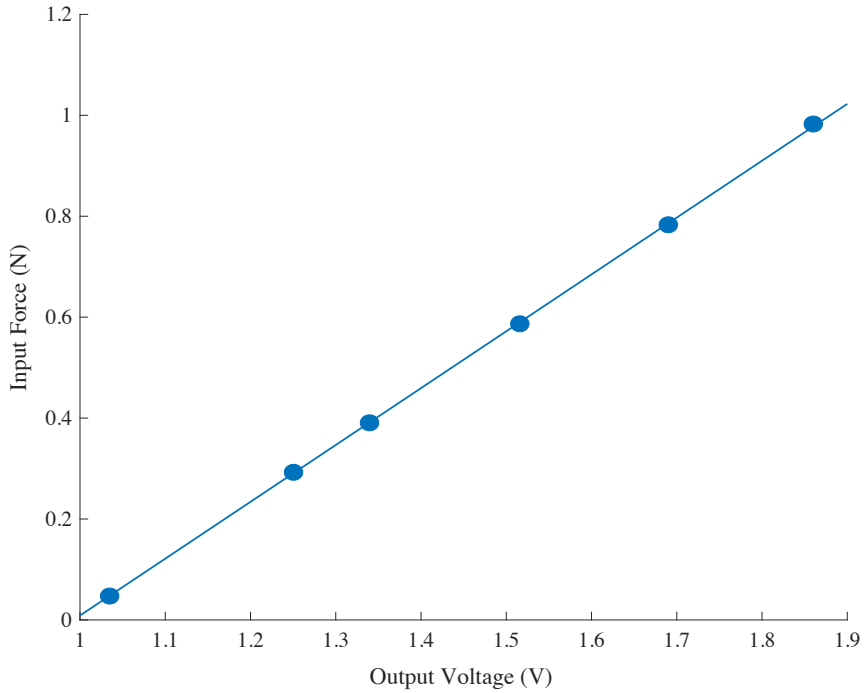

Figure 11: Output voltage vs input force for each mass. The regression is equation y = 1.127x – 1.118 and the coefficient of determination R^2 = 1.

4.1 Hydrogel Scaffold Characterization

Mechanical testing was performed to determine which hydrogel composition best matched the mechanical properties of native oral mucosa. The average storage modulus for the 10%, 20%, and 30% gel compositions were 3233 ± 236.32 Pa, 1767 ± 186.61 Pa, and 1019 ± 142.05 Pa. The storage modulus varied inversely with PEG percentage. A comparison with other results obtained in the literature is shown in Figure 12. The 30% PPG matched the lower range of values obtained by parallel plate rheometer, indentometer, and LSR [1, 11, 19, 24, 25]. The 20% PPG matched the upper range of values acquired by LSR. The 10% PPG exceeded all native tissue values and the

modulus range acquired by TWE was not met by any of the gel compositions [1, 25]. The 30% PPG was therefore the best fit for the storage modulus.

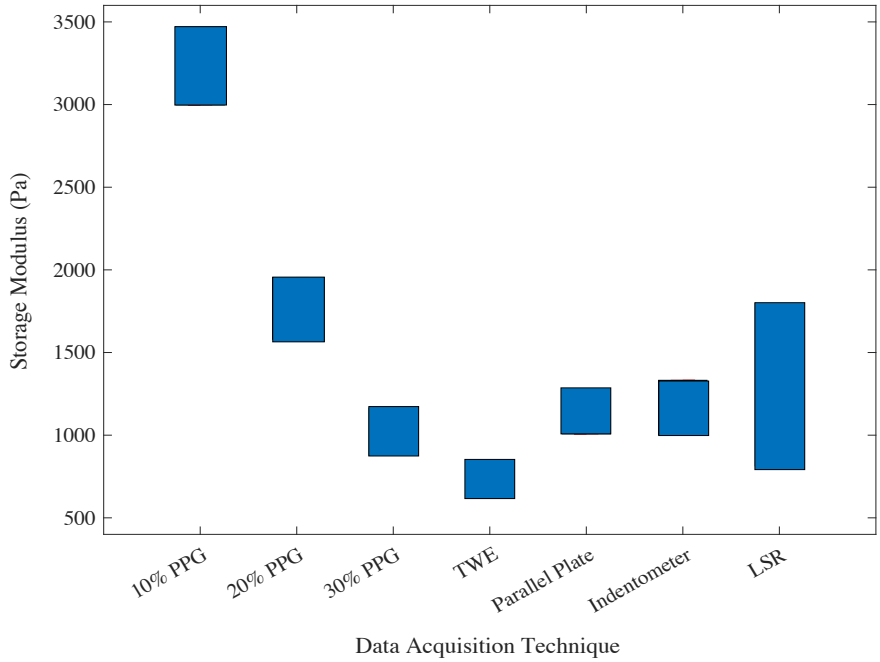

Figure 12: Storage modulus for each PPG gel composition (n = 5) and published storage modulus acquired by TWE, parallel plate, indentometer, and LSR.

The average elastic modulus for the 10%, 20%, and 30% PPG gels were 7.80 ± 0.19 kPa, 4.92 ± 0.12 kPa, and 2.66 ± 0.25 kPa. The elastic modulus scaled inversely with PEG concentration. A comparison between results obtained in this study and values from the literature is shown in Figure 13. All PPG compositions yield a modulus in reasonable agreement. The 30% PPG gel achieved the lower range of values obtained by all acquisition methods [23, 26, 27]. The 20% gel achieved the upper and mid-range of values acquired by indentation and uniaxial traction testing [23, 26]. The modulus of the 10% gel composition matched that of mid-range of values obtained through uniaxial traction testing [26].

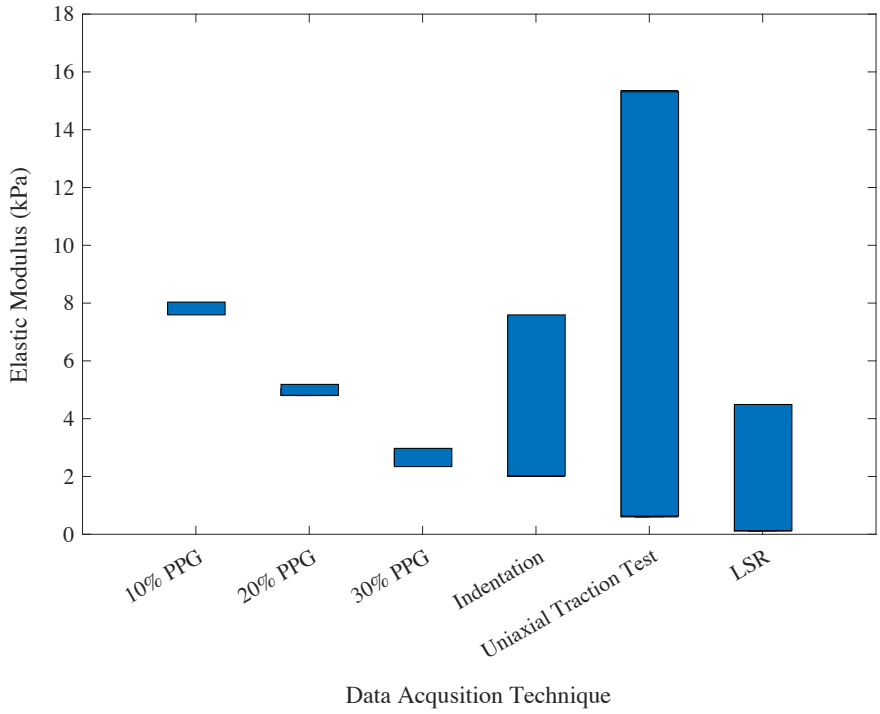

Figure 13: Elastic modulus for each PPG gel composition (n = 5) and published elastic modulus acquired by indentation, uniaxial traction test, and LSR.

Fracture toughness was calculated based on the energy differences between two consecutive needle insertions. A typical force vs time recording of the consecutive insertions is shown in Figure 14A. The signatures of the two insertions are superimposed over and shown in Figure 14B. The force vs time insertion signatures for the first and second insertion were similar. However, the second insertion profile did not include the initial peak in force visible for the first. Instead, the force increased linearly with insertion depth from a zero baseline to a maximum peak. From this point onwards, the second insertion had the same signature as the first. The results therefore indicated that the initial force peak represents the material's deformation upon needle penetration. The force of needle insertion, represented by the second force peak, was roughly equivalent to the

force of deformation for a given insertion. The force of needle insertion was slightly larger for the initial insertion than for the second.

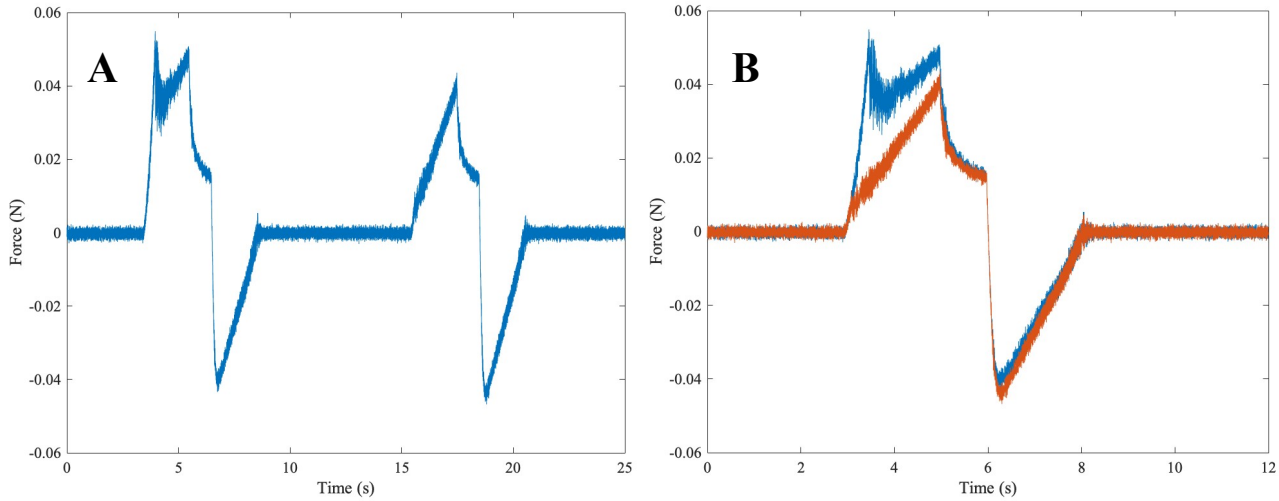

Figure 14: (A) Sample force vs time for consecutive needle insertions. (B) Superimposed force vs time plot depicting initial (blue) and second insertion (orange). Insertion was performed to a depth of 20 mm at a rate of 20mm/s and with a 25G flat tipped needle.

The fracture toughness calculated for each PPG hydrogel was recorded for insertion rates of 5 mm/s, 10 mm/s, and 20 mm/s and needle gauges of 18G, 21G, and 25G, as shown in Figures 15A and 15B. Results showed that the force of both initial and secondary needle insertion scaled with PEG concentration. Forces were largest for the 10% PPG composition, but comparable between the 20% and 30% composition gels. Data outliers for this trend occurred for 18G insertion into the 20% PPG hydrogel and for 10 mm/s insertion into the 10% PPG hydrogel. In addition, fracture toughness was found to increase linearly with needle speed and gauge. This trend applied to all but the 10% gel composition as it had a relatively stable fracture toughness across all gauges. The average fracture toughness across all parameters was 8 J/m^2.

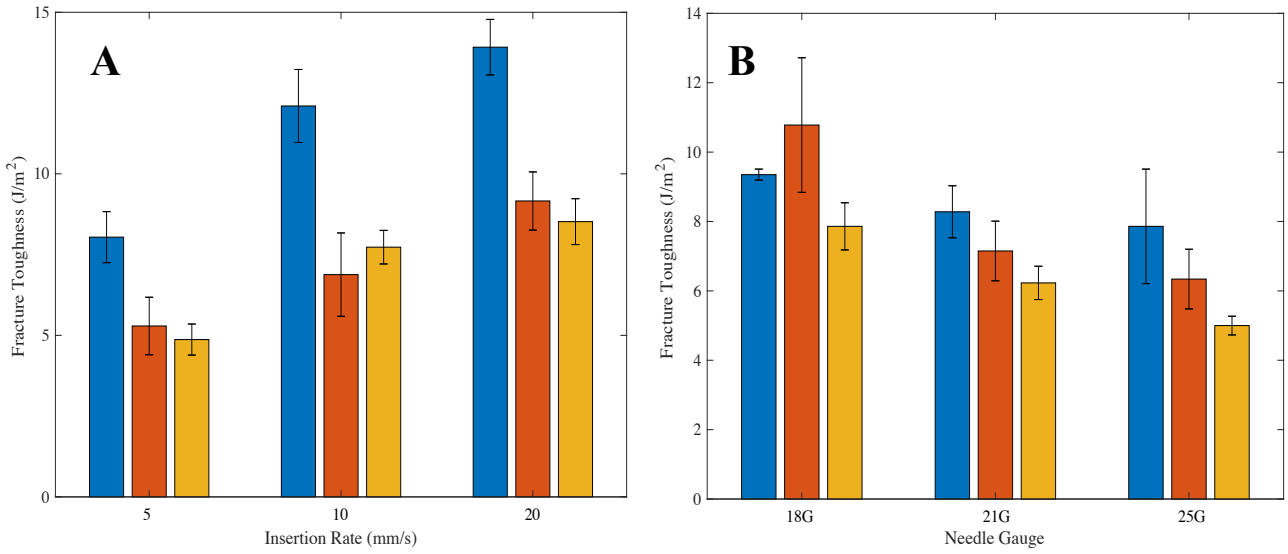

Figure 15: (A) Average fracture toughness for 10% PPG composition (blue), 20% PPG composition (orange), 30% PPG composition (yellow) at varying insertion rates. (B) Average fracture toughness for 10% PPG composition (blue), 20% PPG composition (orange), 30% PPG composition (yellow) at varying needle gauges

A comparison with other results from the literature is shown in Figure 16. Human and porcine tissue fracture toughness were not included in the figure as they greatly exceeded the values for PPG hydrogel [1, 30]. Only the values obtained for gelatin and the network hydrogel materials were plotted. The PPG gels represented the mid-range of the network hydrogel's fracture toughness [29]. The hydrogels also represented the upper range of gelatin's fracture toughness [54]. The 10% PPG gel composition most closely matched values reported for human tissue, as it had a larger fracture toughness than the 20% and 30% compositions.

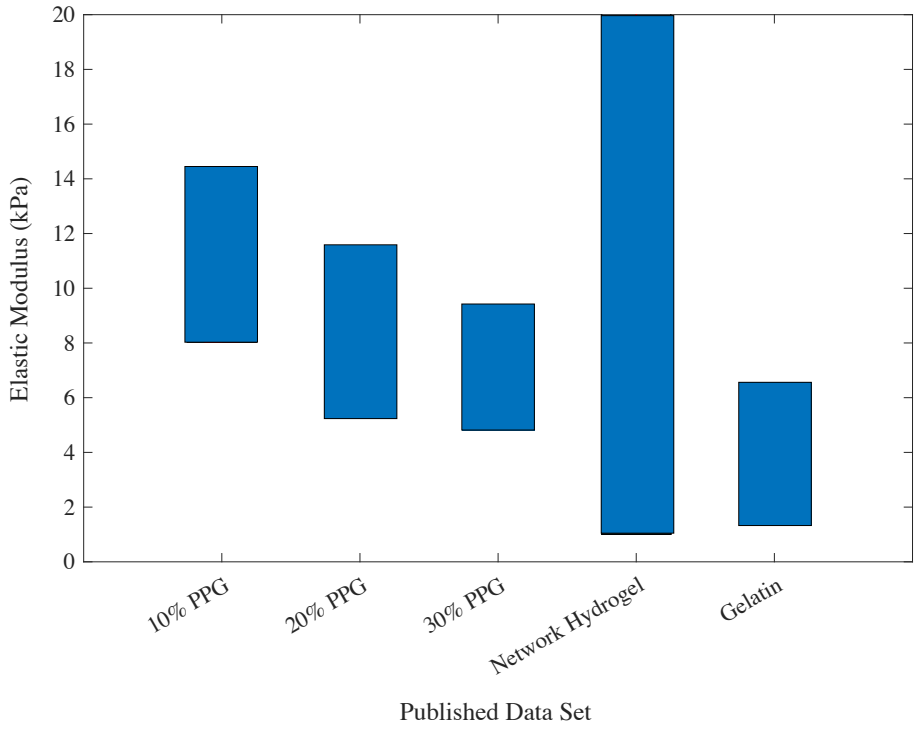

Figure 16: Fracture toughness range for each PPG gel composition (n = 5) and published fracture toughness values of network hydrogel (single and double network) and gelatin.

The results showed that the elastic modulus of all compositions were similar to that of the LP. The fracture toughness of the 10% hydrogel and elastic modulus of the 30% hydrogel were most similar to the range of LP values reported in literature. Porosity analysis was performed on the 10% and 30% gels to further differentiate between them. SEM imaging showed that the 10% gel composition had little to no pores. The only visible pore visible was 61 nm in size. The 30% gel composition had pores of varying sizes, distributed randomly throughout the gel. The maximum, minimum, and average pore size of the 30% PPG hydrogel were 1293 nm, 87 nm, and 553 nm. To verify the effect of porosity on liquid dispersion, injections were performed in both hydrogels. Liquid injected into the 30% PPG gel expanded circumferentially from a point source, as shown in Figure 17C. Injection into the 10% PPG gel fractured the material and spread

vertically, as shown in Figure 17D. The 30% PPG material was therefore selected as the most appropriate hydrogel as it more closely replicated in-vivo liquid dispersion.

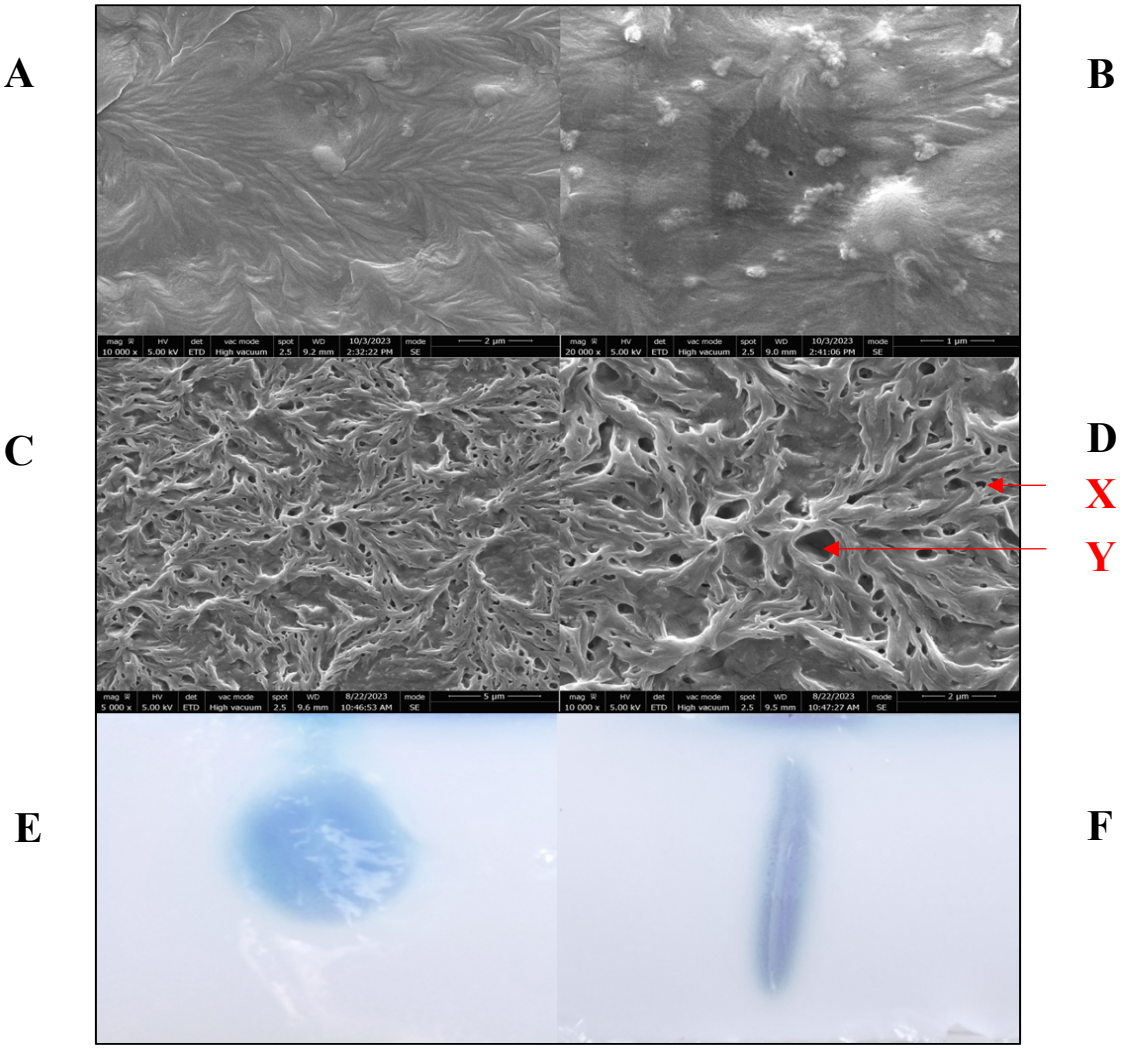

Figure 17: SEM of 10% PPG gel composition shown at magnifications of (A) 10,000x and (B) 20,000x. SEM of 30% PPG gel composition shown at magnifications of (C) 5,000x and (D) 10,000x. The smallest and largest pores are shown by X and Y. Injected liquid dispersion in (E) the 30% PPG hydrogel and (F) the 10% PPG hydrogel. Methylene blue solution was injected at 0.9mL/min, 5mm/s, 0.1 mL, using a 25 G needle.

4.2 Dynamic Analysis

The force vs time histories for needle injection and insertion are shown in Figure 18. Neither signatures followed the trend observed for needle insertions. This could be attributed to differences in needle tip geometry, as the data in Figure 18 was acquired with a bevel tipped, not flat tipped, needle. Needle penetration, relaxation, and withdrawal were observed for both force vs time plots, as reported in the literature [30]. Needle insertion for both profiles was shown by an initial force spike. Once the needles reached their final depth, they remained static, thus the constant force. The injection and insertion histories began to differ from this point forward. The inserted needle maintained a constant force for the entire duration. In contrast, the needle delivering an injection experienced an observable, but statistically insignificant, drop in force at the 11 second mark ($p < 0.05$, $p = 0.310$). A moment of rapid liquid expansion, observed by the experimenter as a burst of blue dye from the tip of the needle, occurred at this exact time point. The reduced force was then maintained for the rest of the injection. Eventually, both needles were removed from the gel, as indicated by the negative force component. The removal force of the injection signature was significantly smaller ($p < 0.05$, $p = 0.027$) than that of the insertion signature, as displayed in Figure 18.

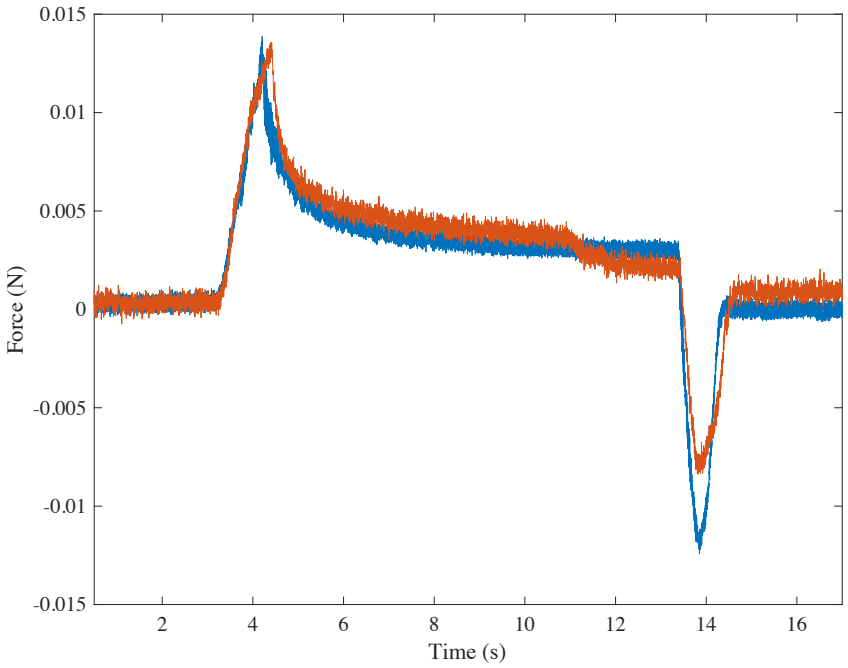

Figure 18: Force-time profile for injection (red) and insertion (blue) performed at a rate of 0.9 mL/min, insertion of 5 mm/s, injection volume of 0.1 mL, and a needle gauge of 25G,

Dynamic analysis of needle injection was explored at injection rates of 0.9 mL/min, 3.6 mL/min, and 7.2 mL/min. These rates represented the upper and lower range of clinical values for superficial soft tissue injection [54]. The force vs time profiles recorded for each injection rate are shown in Figure 19. The force and time magnitudes extracted from the recordings are shown in Figure 20 and Figure 21. Results showed that variation in injection rate did not impact F_I, F_X, or F_R. F_I and F_R remained consistent at approximately 0.014 ± 0.0005 N and 0.010 ± 0.0008 N. All F_X values reached a final magnitude of 0.002 ± 0.0003 N, although injections delivered at a higher rate reached a constant value in a shorter time period. The injection rate varied with the inverse of the injection period, T_T, due to a decrease in T_X.

The stagnation pressure and force were calculated for each injection rate to provide insight on the lack of F_X variation. The stagnation pressure for the 0.9 mL/min, 3.6 mL/min, and 7.2 mL/min injections were $1.83 \bullet 10^{-5}$ Pa, $3.00 \bullet 10^{-4}$ Pa, and $1.00 \bullet 10^{-3}$ Pa. The stagnation force for the 0.9 mL/min, 3.6 mL/min, and 7.2 mL/min injections were $3.88 \bullet 10^{-12}$ N, $6.36 \bullet 10^{-11}$ N, and $2.33 \bullet 10^{-9}$ N. The stagnation forces were 10^{6}-10^{10} times smaller than F_I and F_R. As a result, variation in stagnation force was likely too small to be registered by the force gauge transducer.

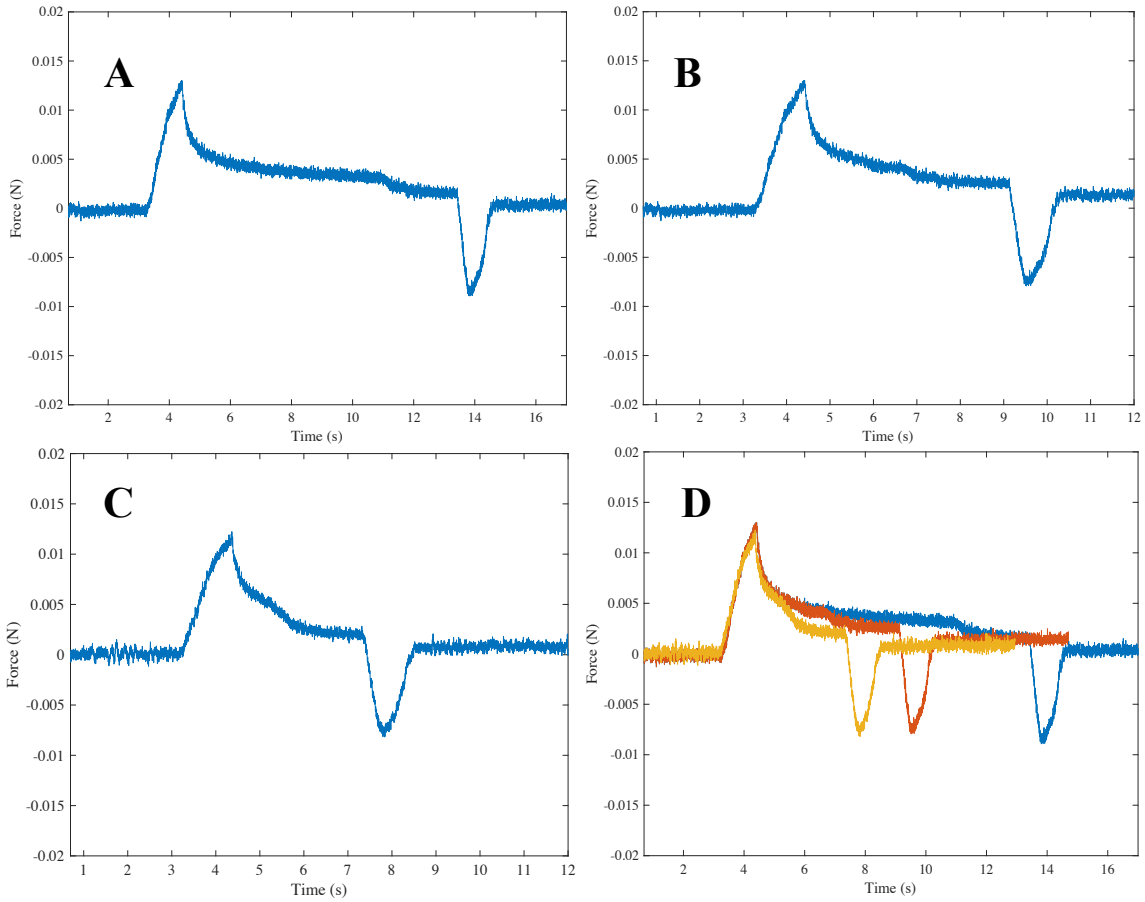

Figure 19: Force vs time histories of needle injection at injection rates of (A) 0.9 mL/min, (B) 3.6 mL/min, and (C) 7.2 mL/min. (D) Overlay of histories at 0.9 mL/min (blue), 3.6 mL/min (orange), and 7.2 mL/min (yellow). Methylene blue solution was delivered at an insertion of 5 mm/s, volume of 0.1 mL, and the needle gauge was 25G.

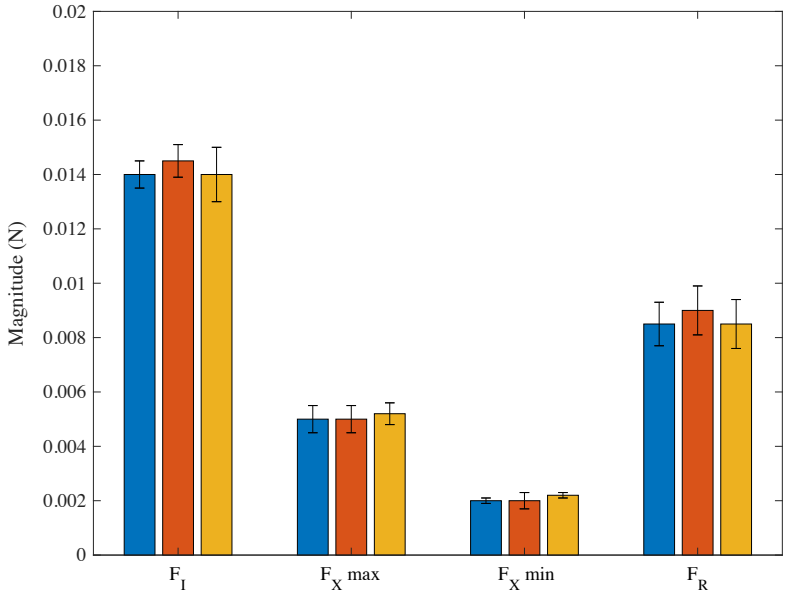

Figure 20: Magnitude of needle insertion force (F_I), maximum injection force (F_X max), minimum injection force (F_X min), and needle removal force (F_R) at injection rates for 0.9mL/min (blue), 3.6mL/min (orange), and 7.2mL/min (yellow).

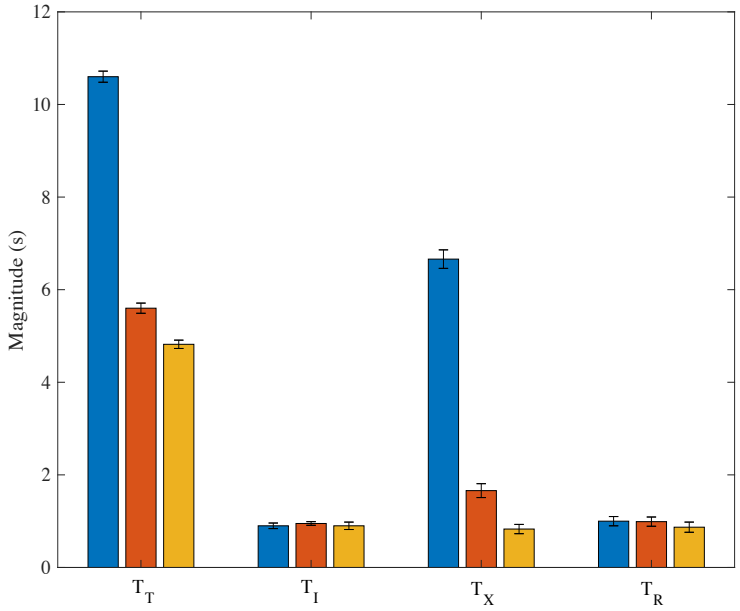

Figure 21: Magnitude of total duration time (T_T), needle insertion duration (T_I), injection duration (T_X), and needle removal duration (T_R) at injection rates of 0.9mL/min (blue), 3.6mL/min (orange), and 7.2mL/min (yellow).

Needle injection was explored for insertion rates of 5 mm/s, 10 mm/s, and 20 mm/s. As for the injection rate, the insertion speed was selected based on clinical relevance [54]. The force vs time profiles, as well as the associated force and time peak magnitudes values, are shown in Figures 22, 23, and 24. Results indicated that a variation in insertion rate had a slight correlation with F_I. The force F_I increased from 0.014 ± 0.0008 N to 0.016 ± 0.0007 N as the insertion rate was increased from 5 mm/s to 20 mm/s. A correlation was observed between the rate of needle insertion and F_R. The F_R increased significantly from 0.010 ± 0.0008 N to 0.018 ± 0.0005 N ($p < 0.05$, $p = 0.012$) as the rate of removal increased from 5 mm/s to 20 mm/s. The liquid dispersion profiles for each insertion rate were analyzed, as described in section 4.4.1, to better understand this trend. The insertion rate was inversely correlated with T_T due to a decrease in T_I and T_R.

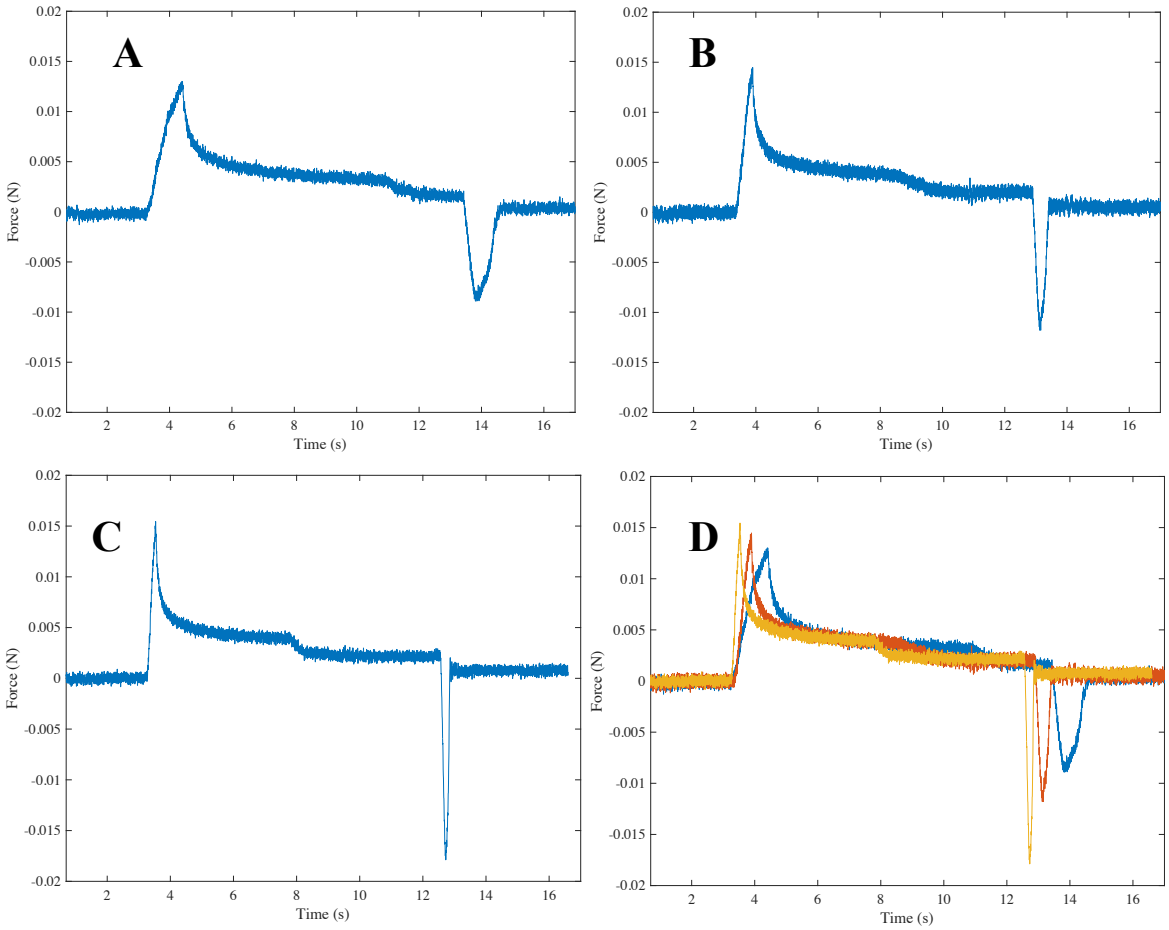

Figure 22: Force vs time histories of needle injection at insertion rates of (A) 5mm/s, (B) 10 mm/s, and (C) 20mm/s. (D) The overlaid histories at 5 mm/s (blue), 10 mm/s (orange), and 20 mm/s (yellow). Methylene blue solution was delivered at a rate of 0.9mL/min, volume of 0.1 mL, and the needle gauge was 25G.

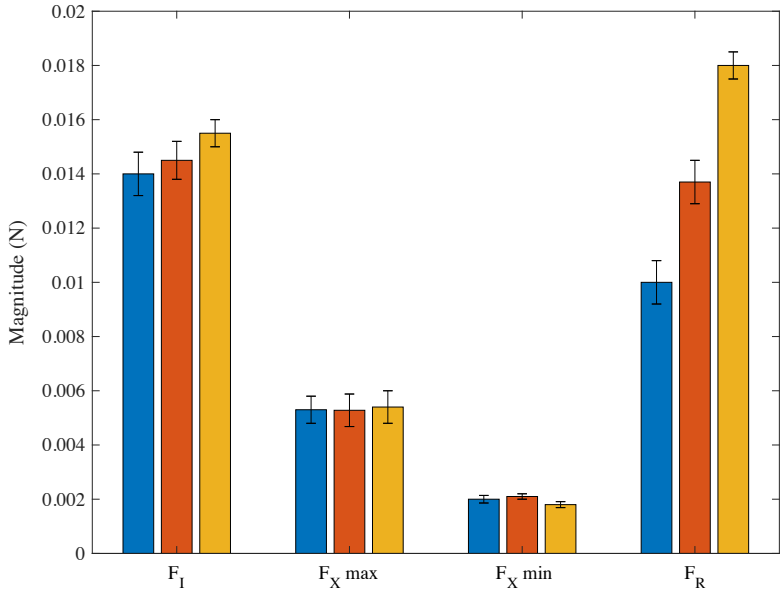

Figure 23: Magnitude of needle insertion force (F_I), maximum injection force (F_X max), minimum injection force (F_X min), and needle removal force (F_R) at insertion rates of 5 mm/s (blue), 10mm/s (orange), and 20 mm/s (yellow).

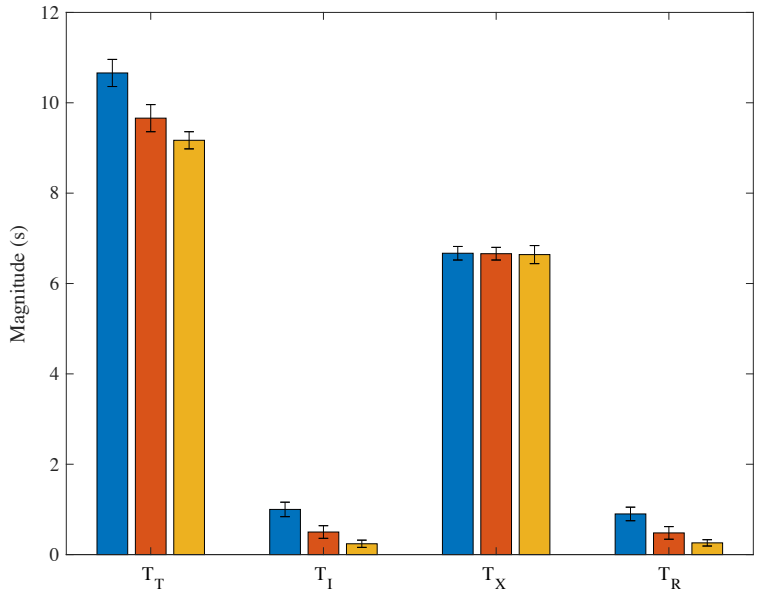

Figure 24: Magnitude of total duration time (T_T), needle insertion duration (T_I), injection duration (T_X), and needle removal duration (T_R) at insertion rates of 5 mm/s (blue), 10mm/s (orange), and 20 mm/s (yellow).

The effect of liquid volume on needle injection dynamics was explored for volumes. Fluid volumes of 0.05 mL, 0.1 mL, and 0.2 mL were selected based on typical dosages for vocal fold injection and adjusted to fit the dimensions of the PPG hydrogel [20, 64-67]. The force vs time profiles recorded for each liquid volume are shown in Figure 25. As shown in Figure 26, the force F_X was significant with liquid volume. As the liquid volume increased from 0.1 mL to 0.2 mL, F_X began to increase rather than decrease overtime. Interestingly, the force F_X max for the 0.2 mL volume was observed at the end of injection. This trend was not observed for the 0.05 mL and 0.1 mL injections, and could therefore be attributed to an increase in hydrodynamic pressure. In contrast, F_R was significantly smaller for the 0.2 mL injection than for other volumes ($p < 0.05$, $p = 0.006$). The dispersion profiles were analyzed in section 4.4.1 to better understand this trend. Lastly, an increase in injection volume increased T_T due to variation in $T_{X,}$ as shown in Figure 27.

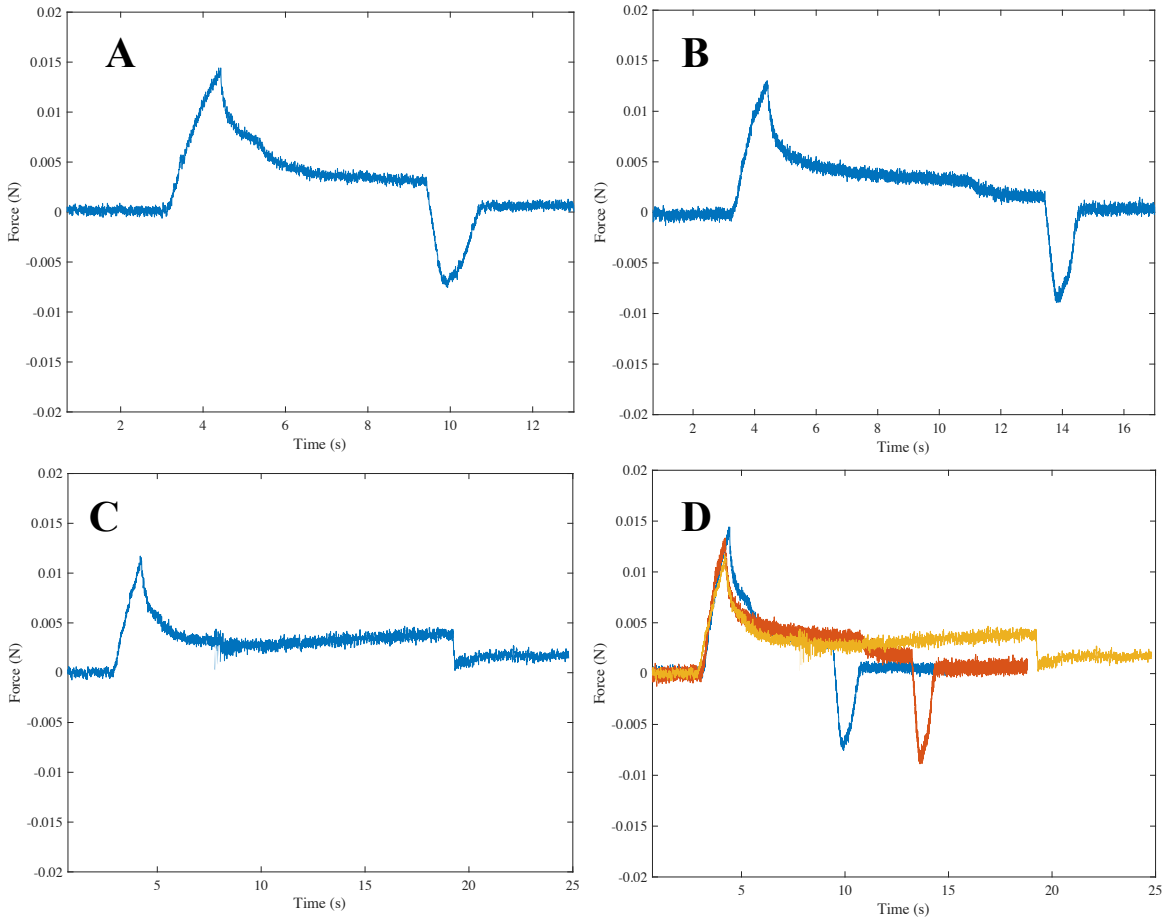

Figure 25: Force vs time histories of needle injection at injection volumes of (A) 0.05 mL, (B) 0.1 mL, and (C) 0.2 mL (C). (D) The combined histories at 0.05 mL (blue), 0.1 mL (orange), and 0.02 mL (yellow). Methylene blue solution was delivered at a rate of 0.9mL/min, insertion of 5 mm/s, and the needle gauge was 25G.

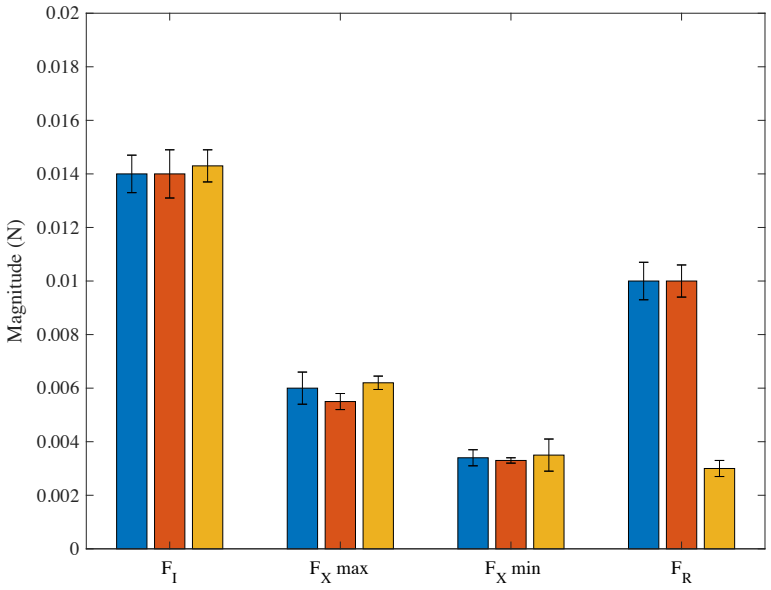

Figure 26: Magnitude of needle insertion force (F_I), maximum injection force (F_X max), minimum injection force (F_X min), and needle removal force (F_R) at injection volumes of 0.05mL (blue), 0.1mL (orange), and 0.2mL (yellow).

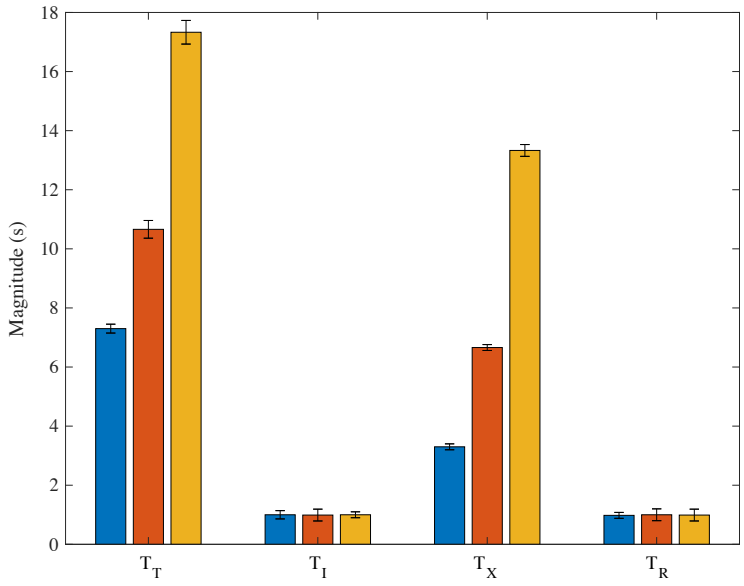

Figure 27: Magnitude of total duration time (T_T), needle insertion duration (T_I), injection duration (T_X), and needle removal duration (T_R) at injection volumes of 0.05mL (blue), 0.1mL (orange), and 0.2mL (yellow).

Needle injection was performed using gauges of 23G, 25G, and 27G. Gauge selection was based on published clinical procedures for lamina propria injection [20, 64-67]. The force vs time profiles recorded for each gauge are shown in Figure 28. As shown in Figure 29, F_I and F_R were greatly impacted by needle gauge. The F_I was inversely proportional to needle gauge, decreasing from 0.018 ± 0.0010 N to 0.006 ± 0.0005 N as the needle gauge progressed from 23G to 27G. The reduced force at a larger gauge, and smaller needle diameter, was likely due to contact area with the gel surface. In addition, the force F_R had a parabolic relationship with needle gauge. The F_R increased from 0.003 ± 0.0000 N to 0.009 ± 0.0006 N as needle gauge increased from 23G to 25G. The F_R then decreased to 0.001 ± 0.0002 N as needle gauge was increased to 27G. It is likely that the 23G needle created a large hole that it could easily be removed from while the 27G needle was small enough to leave the hole with little force. The 25G needle had the greatest removal force because it existed between each extreme. As shown in Figure 30, variation in needle gauge showed no change in injection duration (T_T).

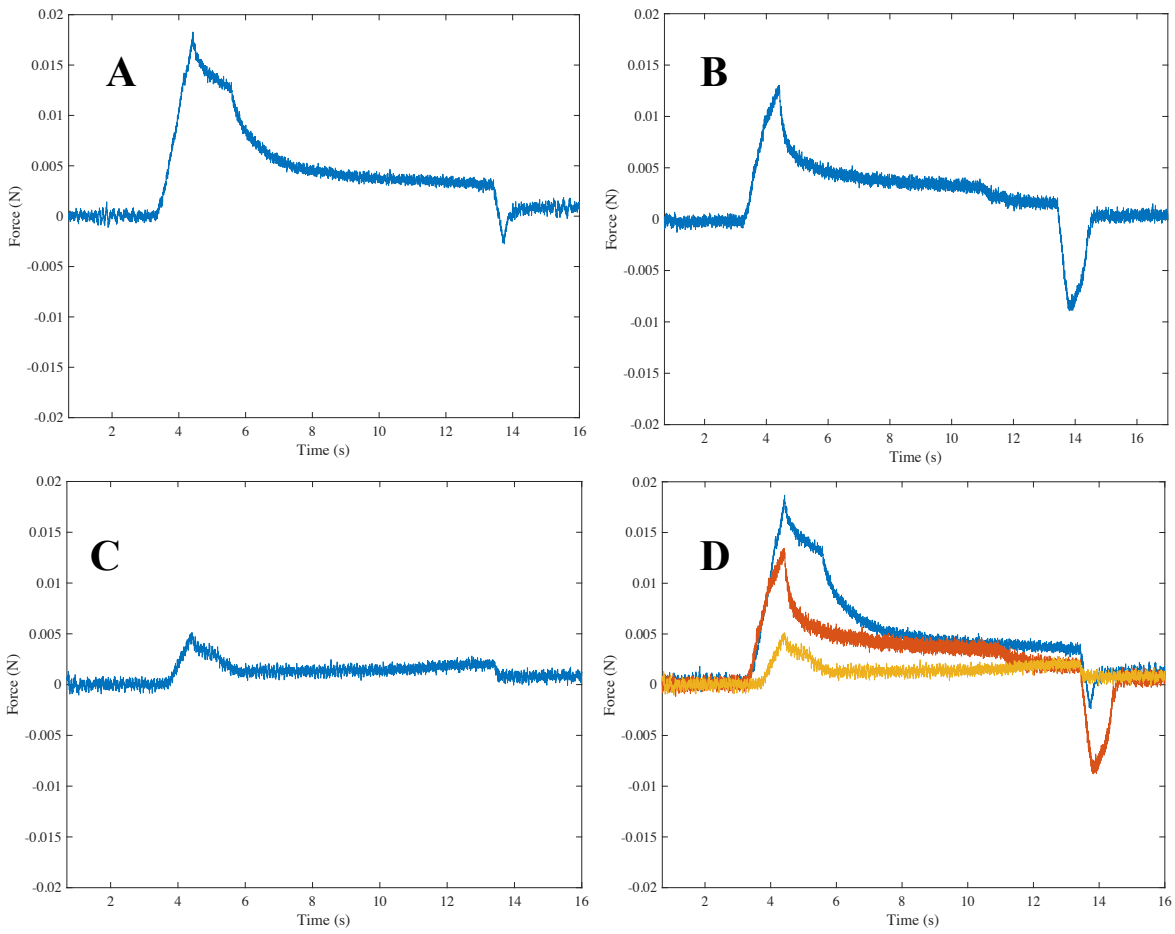

Figure 28: Force vs time histories of needle injection at needle gauges of (A) 23G, (B) 25G, and (C) 27G. (D) The combined histories at 23G (blue), 25G (orange), and 27G (yellow). Methylene blue solution was delivered at a rate of 0.9mL/min, insertion of 5 mm/s, and volume of 0.1 mL.

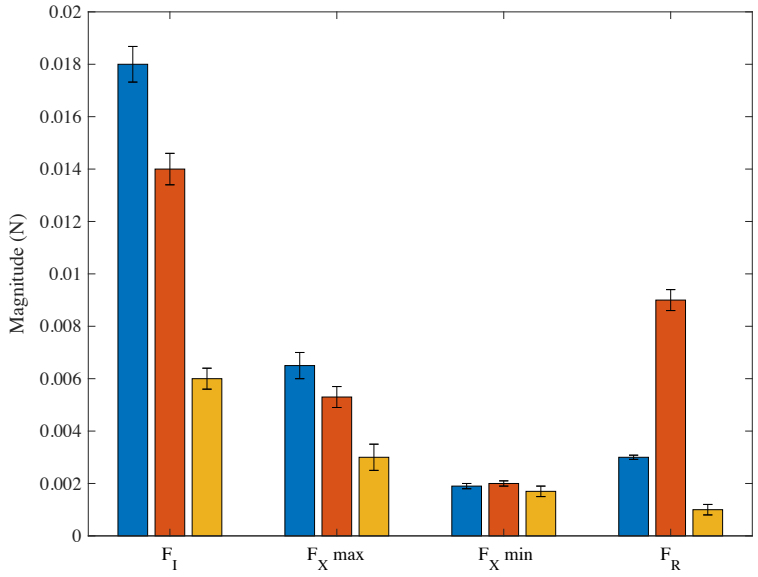

Figure 29: Magnitude of needle insertion force (F_I), maximum injection force (F_X max), minimum injection force (F_X min), and needle removal force (F_R) at needle gauges of 23G (blue), 25G (orange), and 27G (yellow).

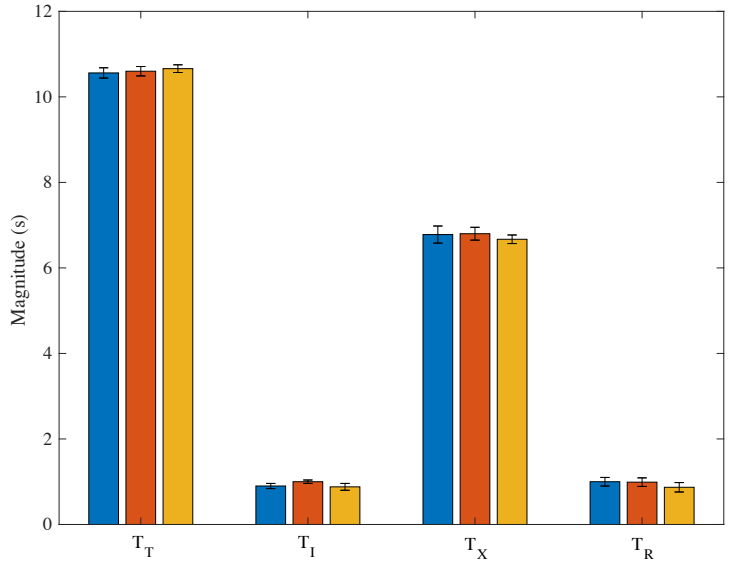

Figure 30: Magnitude of total duration time (T_T), needle insertion duration (T_I), injection duration (T_X), and needle removal duration (T_R) at needle gauges of 23G (blue), 25G (orange), and 27G (yellow).

The dynamic response of NFLJI was measured at various driving pressures. The device's lowest operating pressure, 275 kPa, was selected to match the small force of needle injection. Larger driving pressures of 448 kPa and 620 kPa were selected based on their use in other NFLJI studies [54]. The force vs time profiles, as well as maximum force and time magnitudes, are shown in Figure 31, Table 5, and Table 6. The forces $F_{max}+$ and $F_{max}-$ occurred at initial impact and scaled proportionally with driving pressure. The greatest and smallest $F_{max}+$ were 0.12 ± 0.0400 N at 275 kPa and 0.26 ± 0.0300 N at 620 kPa. The greatest and smallest $F_{max}-$ were 0.06 ± 0.0300 N at 275 kPa and 0.08 ± 0.0300 N at 620 kPa. A small y-axis jump at initial contact was observed for each profile before the force amplitude exponentially decayed. This jump likely indicated the strength of the injection and the net positive momentum it created. Results further showed that driving pressure was proportional to T_T. The maximum and minimum T_T values were 0.59 ± 0.0892 s at 275 kPa and 0.35 ± 0.0084 s at 620 kPa.

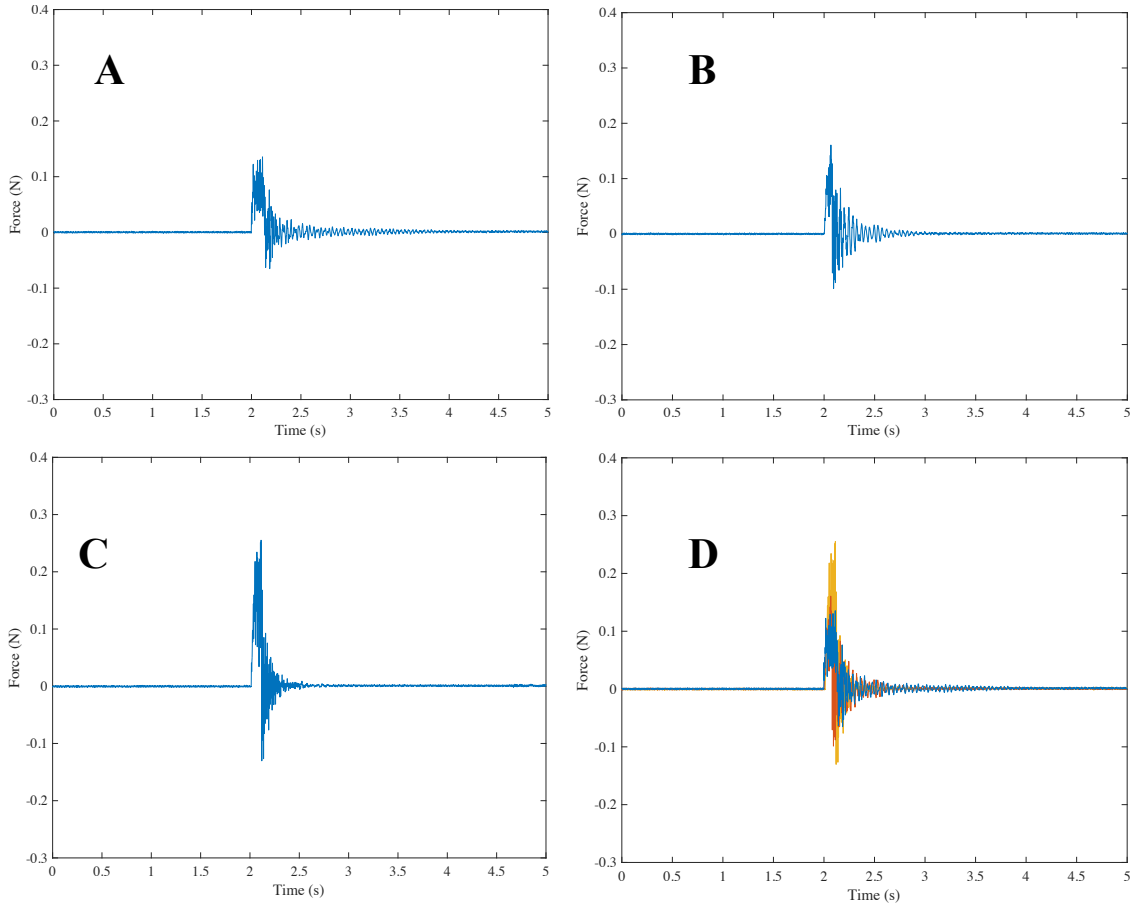

Figure 31: Force vs time histories of NFLJI at driving pressures of (A) 275 kPa, (B) 448 kPa, and (C) 620 kPa. (D) The combined histories of the 275 kPa (blue), 448 kPa (orange), and 620 kPa (yellow) driving pressures. A volume of 0.1 mL methylene blue solution was delivered.

Table 5: Magnitude of maximum injection force in the positive (F_{max}+) and negative (F_{max} -) direction for driving pressures of 275 kPa, 448 kPa, and 620 kPa.

	F_{max}+ (N)	**F_{max} – (N)**
275 kPa	0.12 ± 0.0400	0.06 ± 0.0275
448 kPa	0.18 ± 0.0208	0.07 ± 0.0203
620 kPa	0.26 ± 0.0311	0.08 ± 0.0367

Table 6: Magnitude of total injection duration (T_T) at driving pressures of 275 kPa, 448 kPa, and 620 kPa.

	T_T (s)
275 kPa	0.59 ± 0.0892
448 kPa	0.52 ± 0.0544
620 kPa	0.35 ± 0.0084

The effect of volume on NFLJI dynamics was investigated for volumes of 0.05 mL, 0.1 mL, 0.2 mL. The injection volumes were selected to match those used for needle injection, and to therefore replicate clinically relevant values. The force vs time profiles recorded for injection rate are shown in Figure 32. Peak force and time magnitudes from the recordings are shown in Table 7 and Table 8. Similar to variation in driving pressure, the force F_{max}+ and F_{max}- occurred during initial impact. The greatest and smallest F_{max}+ were 0.1 ± 0.0100 N at 0.05 mL and 0.3 ± 0.0300 N at 0.2 mL. The greatest and smallest F_{max}- were 0.05 ± 0.0100 N at 0.05 mL and 0.22 ± 0.0200 N at 0.2mL. No y-axis jump or significant change in injection duration was observed between liquid volumes.

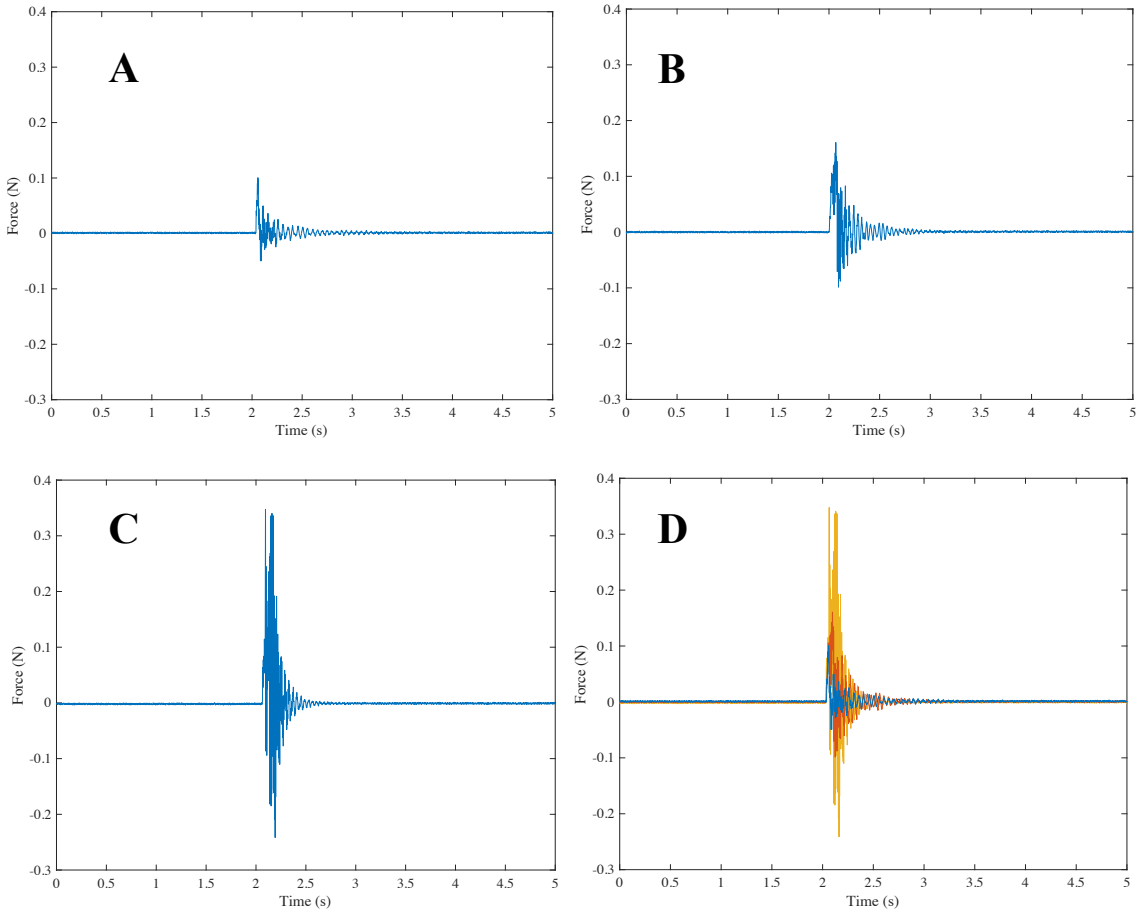

Figure 32: Force vs time histories of NFLJI at liquid volumes of (A) 0.05 mL, (B) 0.1 mL, and (C) 0.2 mL. (D) The combined histories of the 0.05 mL (blue), 0.1 mL (orange), and 0.2 mL (yellow) injection volumes. Methylene blue solution was delivered at a driving pressure of 448 kPa.

Table 7: Magnitude of maximum injection force in the positive (F_{max}+) and negative (F_{max} -) direction for liquid volumes of 0.05 mL, 0.1 mL, and 0.2 mL (n = 3).

	F_{max}+ (N)	**F_{max} – (N)**
0.05 mL	0.10 ± 0.0080	0.05 ± 0.0078
0.1 mL	0.18 ± 0.0208	0.07 ± 0.0173
0.2 mL	0.33 ± 0.0311	0.22 ± 0.0180

Table 8: Magnitude of total injection duration (T_T) for injection volumes of 0.05 mL, 0.1 mL, and 0.2 mL (n = 3).

	T_T (S)
0.05 mL	0.49 ± 0.1823
0.1 mL	0.50 ± 0.1256
0.2 mL	0.51 ± 0.1605

The maximum, minimum, and average force of needle and needle-free injection are shown in Table 9. The maximum and minimum force for needle-free injection were 18x and 45x larger than needle injection. The average force of needle-free injection was 17.8x larger than that for needle injection.

Table 9: Maximum, minimum, and average force for needle and needle-free injection (n = 3).

	Maximum Injection Force (N)	**Minimum Injection Force (N)**	**Average Injection Force (N)**
Needle Injection	0.018 ± 0.0005	0.001 ± 0.0002	0.008
Needle-free Injection	0.330 ± 0.0300	0.045 ± 0.0100	0.143

Table 10 shows the time durations for needle and needle-free injection. The maximum and minimum duration for needle-free injection were 29x and 14x smaller than those for needle injection. Overall, the average duration of needle-free injection was 20x smaller than needle injection.

Table 10: Maximum, minimum, and average time duration for needle and needle-free injection (n = 3).

	Maximum Injection Duration (s)	**Minimum Injection Duration (s)**	**Average Injection Duration (s)**
Needle Injection	17.3 ± 0.4000	4.82 ± 0.1000	9.93
Needle-free Injection	0.59 ± 0.1000	0.35 ± 0.0100	0.50

4.3 MORPHOLOGICAL ANALYSIS

Morphological analysis of needle injection was explored at each injection rate. The dispersion profile and morphological parameters are shown in Figure 33 and Figure 34. Results showed that increasing the injection rate increased the injection depth and decreased the injection width. The depth, D_{max}, increased significantly from 12.4 ± 0.2 mm to 18 ± 0.7 mm ($p < 0.05$, $p = 3.90 \bullet 10^{-}$

[6]) and the width, W_{max}, decreased significantly from 8.6 ± 0.7 mm to 6.8 ± 0.3 mm ($p < 0.05$, $p = 0.002$) as injection rate increased from 0.9mL/min to 7.2mL/min. Overall, the dispersion profile transitioned from a shallow and circular to a deep and narrow geometry with increasing injection rate. It is likely that the liquid had more vertical momentum, preventing it from spreading laterally, when introduced into the gel at a faster rate.

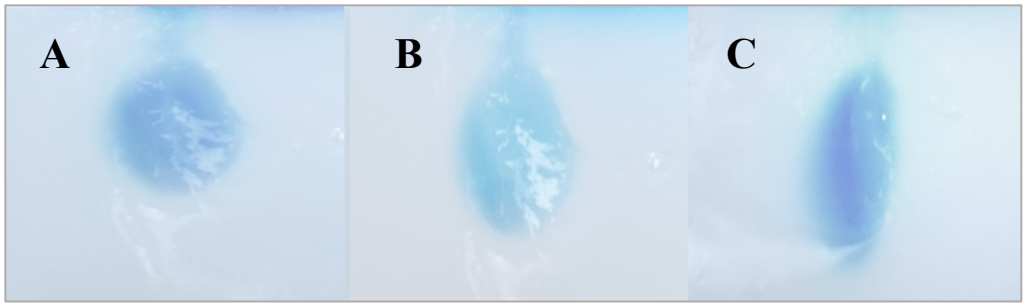

Figure 33: Liquid dispersion profile for fluid delivered at injection rates of (A) 0.9 mL/min, (B) 3.6 mL/min, and (C) 7.2 mL/min.

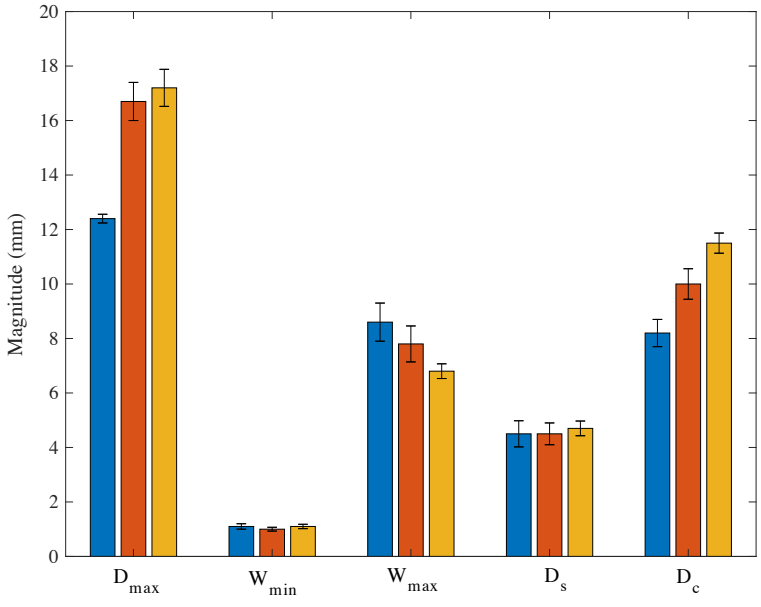

Figure 34: Magnitude of morphological parameters for injection rates of 0.9 mL/min (blue), 3.6 mL/min (orange), and 7.2 mL/min (yellow) (n = 3).

The liquid dispersion profile created by each insertion rate is characterized in Figure 35 and Figure 36. Results showed that variation in insertion rate had the same relationship to injection depth and width as injection rate. The depth, D_{max}, increased significantly from 12.2 ± 0.6 mm to 18 ± 0.7 mm ($p < 0.05$, $p = 9.10 \bullet 10^{-6}$) and the width, W_{max}, decreased significantly from 8.5 ± 0.6 mm to 3 ± 0.3 mm ($p < 0.05$, $p = 4.25 \bullet 10^{-6}$) as insertion rate progressed from 5mm/s to 20mm/s. However, a crack observed at 20 mm/s insertion presented a difference between the injection morphology shown for increasing injection and insertion rates. Liquid regurgitated from the gel at this rate, indicating that the fluid spread up and out of the crack, preventing it from spreading laterally. The loss of liquid led to increased friction and could explain the increase in removal force (F_R) experienced with increasing insertion rate.

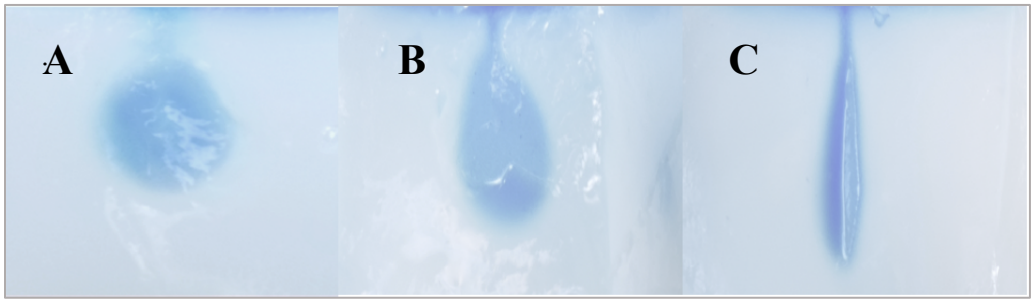

Figure 35: Liquid dispersion profile for fluid delivered at insertion rates of (A) 5 mm/s, (B) 10 mm/s, (C) and 20 mm/s.

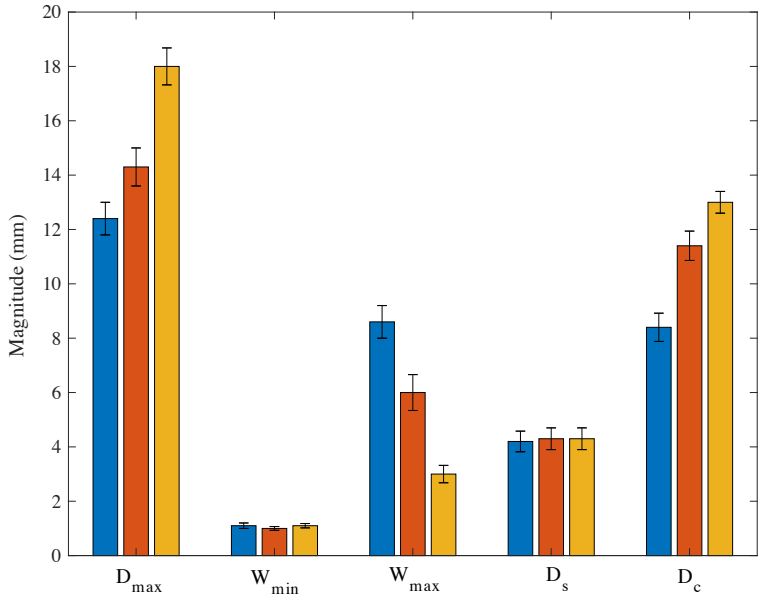

Figure 36: Magnitude of morphological parameter for insertion rates of 5 mm/s (blue), 10 mm/s (orange), and 20 mm/s (yellow (n = 3)).

Injection morphology measured at each injection volume, shown in Figure 37 and 38, revealed that it had proportional relationship to injection depth and width. The dispersion profile expanded circumferentially with increasing volume, maintaining its circular structure. Although the minimum width, W_{min}, did not vary between 0.05 mL and 0.1 mL injection, it was not observed with 0.2 mL of fluid. It is likely that as the liquid bolus expanded to the surface of the hydrogel, the thin vertical line representing needle entry and the smallest injection width was removed. The larger volume led to increased lubrication and hydrodynamic pressure, explaining the increase in injection force (F_X) and decrease in removal force (F_R) experienced with increasing liquid volume.

Figure 37: Liquid dispersion profile for fluid delivered at volumes of (A) 0.05 mL, (B) 0.1 mL, and (C) 0.2 mL.

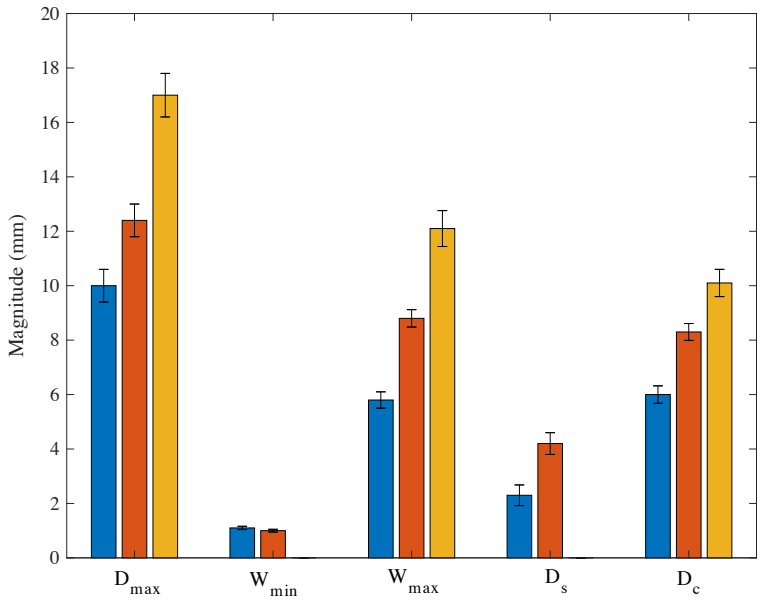

Figure 38: Magnitude of morphological parameter for injection volumes of 0.05mL (blue), 0.1mL (orange), and 0.2mL (yellow) (n = 3).

The impact of needle gauge on injection morphology, shown in Figure 39 and 40, was measured with 23G, 25G, and 27G needles. Results showed that variation in needle gauge did not change injection morphology. Although the standard deviation of dispersion width and depth allowed for slight variations in morphology, as seen between Figure 43, the average values were consistent.

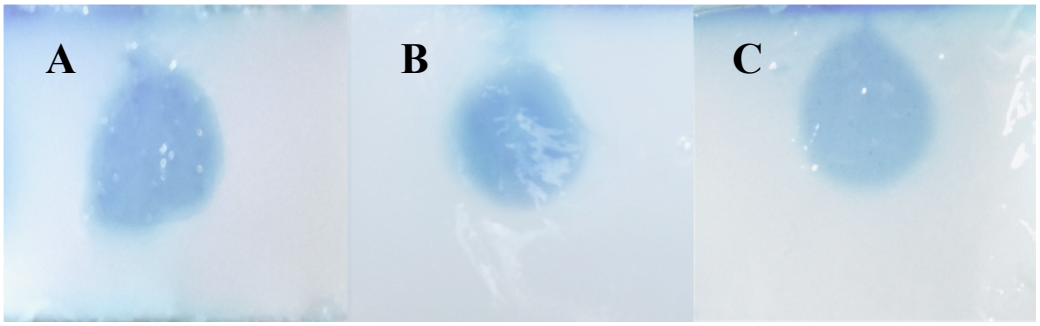

Figure 39: Liquid dispersion profile for fluid delivered at needle gauges of (A) 23G, (B) 25G, and (C) 27G.

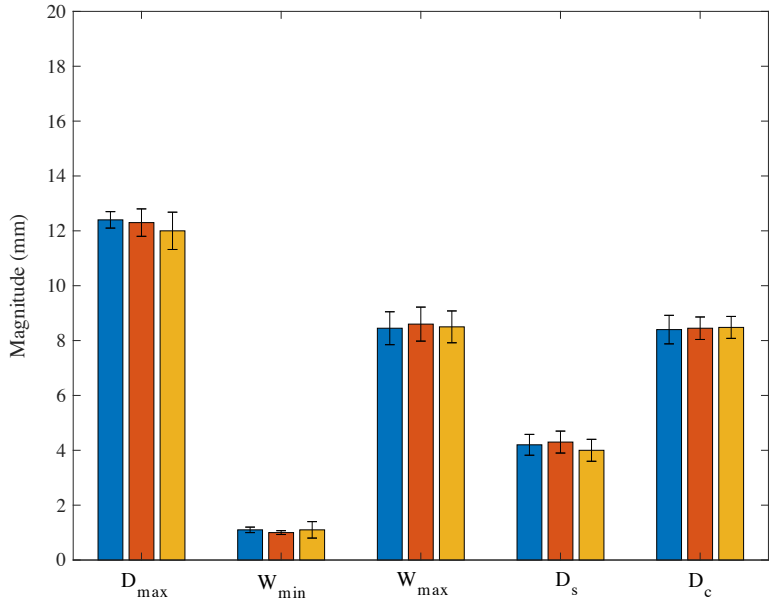

Figure 40: Magnitude of morphological parameter for needle gauges of 23G (blue), 25G (orange), and 27G (yellow) (n = 3).

Dispersion morphology at driving pressures of 275 kPa, 448 kPa, and 620 kPa were measured. Results, as shown in Figure 41 and 42, revealed that variation in driving pressure had a proportional relationship to the depth of injection and an inversely proportional relationship to the width of injection. The dispersion profile of injection had a thin initial shaft that elongated into a circular liquid region. The width of the shaft decreased while the length of the shaft increased with driving pressure. The maximum depth achieved by driving pressures of 448 kPa and 620 kPa consistently

exceeded the hydrogel scaffold depth (20 mm). Depth D_{max} increased significantly from 18 ± 1.0 mm to 38 ± 1.0 mm ($p < 0.05$, $p = 1.08 \bullet 10^{-7}$) as driving pressure increased from 275 kPa to 620 kPa. Widths W_{max} and W_{min} decreased significantly from 10.8 ± 1.2 mm to 8.2 ± 1.0 mm and 5.5 ± 1.0 mm to 3.8 ± 1.1 mm ($p < 0.05$, $p = 0.009$) as driving pressure increased from 275 kPa to 620 kPa.

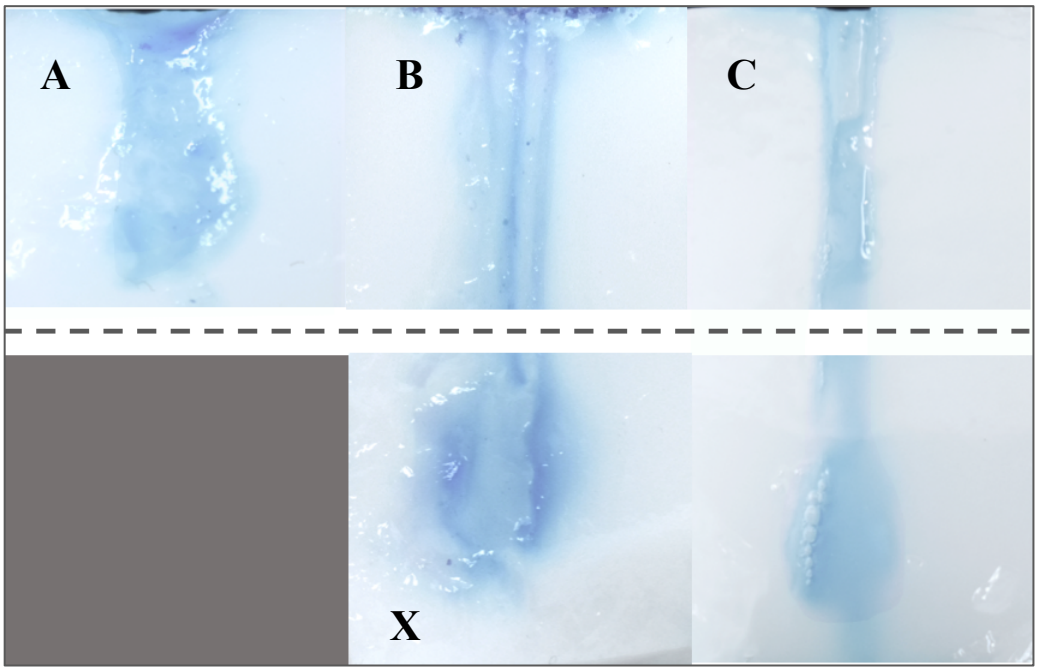

Figure 41: Liquid dispersion profile for fluid delivered at driving pressures of (A) 275 kPa, (B) 448 kPa, and (C) 620 kPa. The dotted horizontal line indicates the 20 mm hydrogel depth. The total distance from (B) to (X) is 40 mm deep.

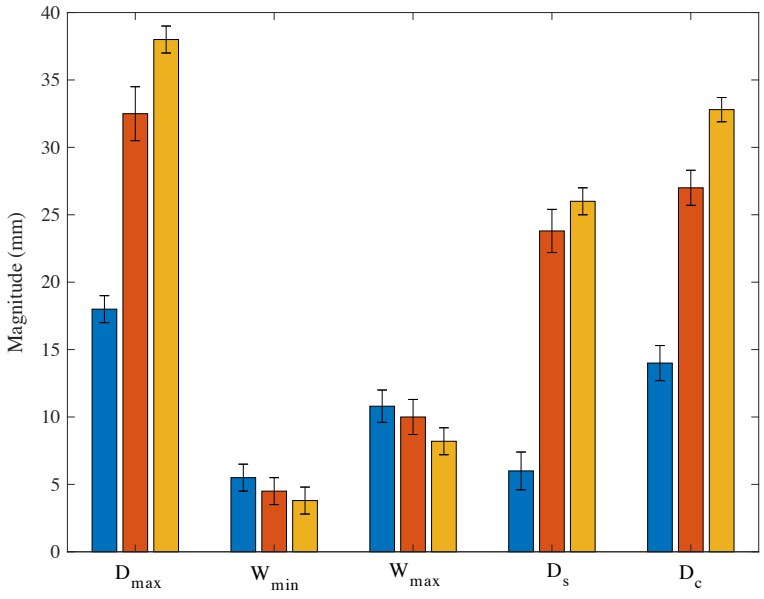

Figure 42: Magnitude of morphological parameter for driving pressures of 275 kPa (blue), 448 kPa (orange), and 620 kPa (yellow) (n = 3).

The effect of liquid volume on NFLJI dispersion morphology is shown in Figure 43 and 44. Increasing liquid volume increased the depth of injection without significantly changing the width. The dispersion profile was a uniform cylindrical shaft. Tearing of the hydrogel was observed for the 0.2 mL injection, likely indicating the turbulent nature of larger liquid volumes. Injection depth D_{max} increased significantly from 11 ± 0.8 mm to <40 mm ($p < 0.05$, $p = 5.37 \bullet 10^{-10}$) as the liquid volume increased from 0.05 mL to 0.2 mL. The maximum depth for liquid volumes of 0.1 mL and 0.2 mL exceeded the hydrogel phantom (20 mm) each time. Injection widths were kept fairly consistent.

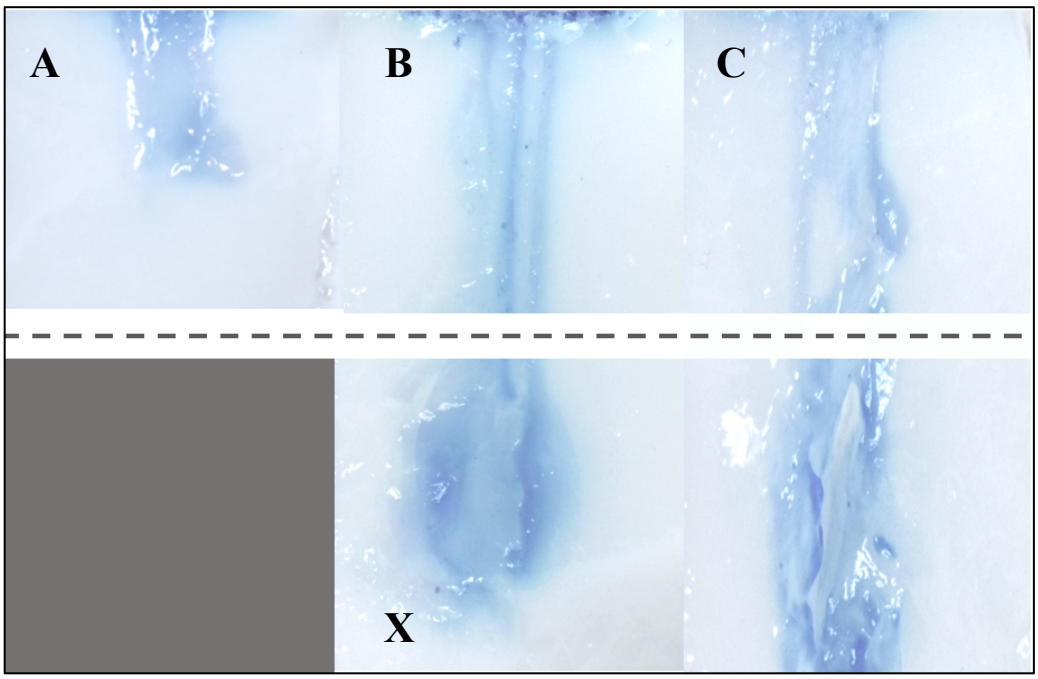

Figure 43: Liquid dispersion profile for delivered liquid volumes of (A) 0.05 mL, (B) 0.1 mL, and (C) 0.2 mL. The dotted horizontal line indicates a 20 mm hydrogel depth. The total depth for (B) to (X) was the 40 mm hydrogel depth.

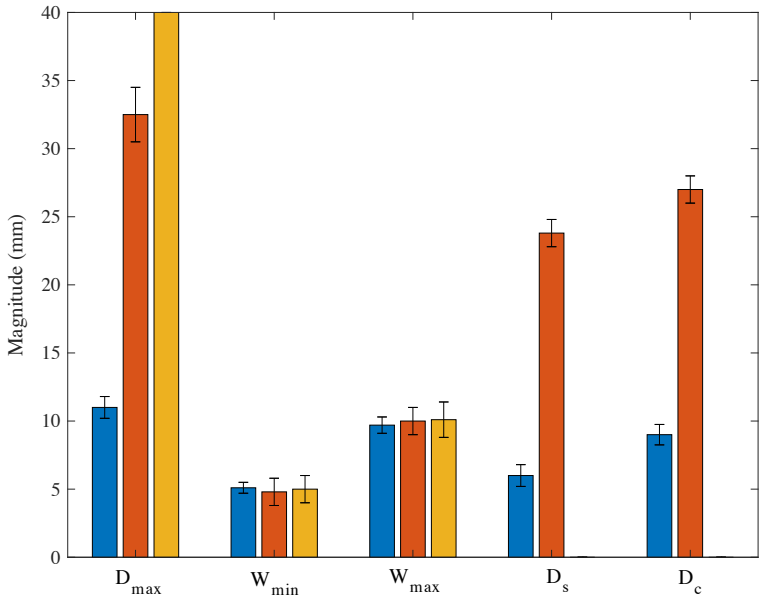

Figure 44: Magnitude of morphological parameter for injection volumes of 0.05mL (blue), 0.1mL (orange), and 0.2mL (yellow) (n = 3).

The maximum, minimum, and average depth recorded across all injection methods are shown in Table 11. The maximum and minimum depth for needle-free injection was infinitely and 10x larger than needle injection, respectfully. On average, the dispersion depth for needle-free injection was 1.9x larger than needle injection.

Table 11: Maximum, minimum, and average depth of needle and needle-free injection (n = 3).

	Maximum Injection Depth (mm)	**Minimum Injection Depth (mm)**	**Average Injection Depth (mm)**
Needle Injection	18 ± 0.7	10 ± 0.6	14.5
Needle-free Injection	< 40	11 ± 0.8	28.1

The width of needle and needle-free injection profiles are shown in Table 12. The maximum injection width was 1.1x larger for needle injection. The minimum injection width was 8.2x larger for needle-free injection. The average width of injection was 1.7x larger for needle-free injection.

Table 12: Maximum, minimum, and average width of needle and needle-free injection (n =3).

	Maximum Injection Width (mm)	**Minimum Injection Width (mm)**	**Average Injection Width (mm)**
Needle Injection	12.1 ± 0.6	1.0 ± 0.1	4.2
Needle-free Injection	10.8 ± 1.2	8.2 ± 1.0	7.3

4.4 Cellular Viability Analysis

A cell viability assay was performed for the 30% PPG gel. Cell preparation was performed as described in section 3.6.2. The cell viability results are shown in Figure 45. The cell viabilities of the control and 30% PPG sample were 98 ± 2 % and 92 ± 3%. A t-test revealed that there was a significant difference between the two values ($p < 0.05$, $p = 0.014$). Although the cell viability was larger for the control sample, the PPG hydrogel sample was still considered cytocompatible. In addition, the PPG sample appeared to have a smaller cell density than the control sample. This can be attributed to cells being integrated throughout the thickness of the material, not just along its superficial surface.

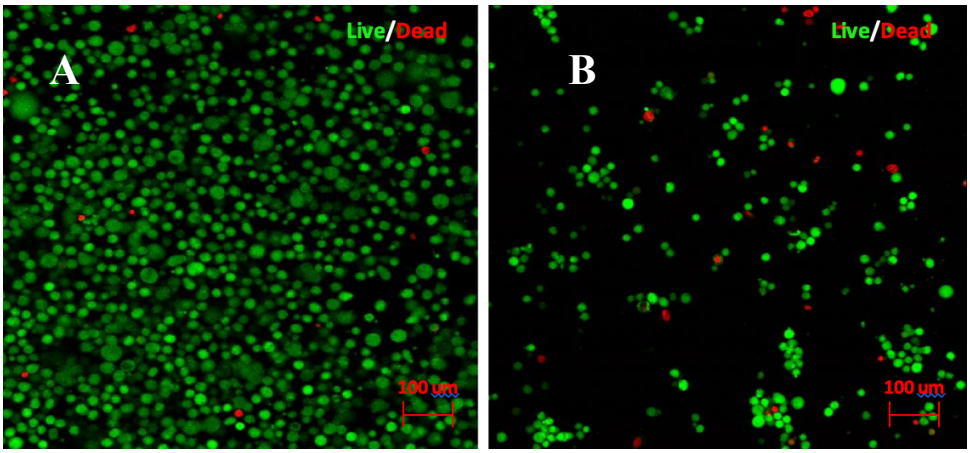

Figure 45: Cell viability for (A) non-PPG control and (B) cell viability for 30% PPG hydrogel.

The cell viability for the 30% PPG control sample and an injected 30% PPG sample were compared. The needle's injection parameters were selected to best represent clinical in-vitro conditions. Typical images of each sample are shown in Figure 46. The cell viabilities were 97% ± 2 and 71% ± 12. A t-test run between the two samples revealed that there was a significant difference in values ($p < 0.05$, $p = 0.006$). Cell density and distribution were consistent between samples. The distribution and position of cells in the injected PPG hydrogel did not indicate the presence of a material void.

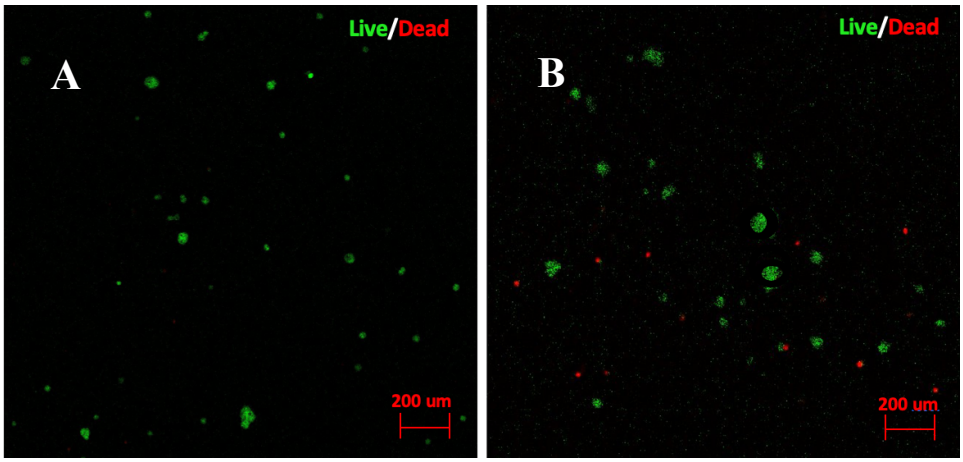

Figure 46: Cell viability for (A) non-injected 30% PPG control and (B) for injected 30% PPG hydrogel. Injections were administered at an injection rate of 0.9 mL/min, insertion rate of 5 mm/s, volume of 0.1 mL, and 25G needle gauge.

Cell viability data for a 30% PPG control sample and an injected 30% PPG sample are shown in Figure 47. The needle-free injection parameters were selected to best mimic the needle's operating conditions. The control sample and the injected sample had average cell viabilities of 97% ± 2 and 65% ± 15. A significant difference between the two samples existed ($p < 0.05$, $p = 0.007$). The density and distribution of cells were similar between samples. In contrast to needle insertion, the injected liquid's site of entry left a material void too large to be captured by the microscope's field of view. As such, images were taken around the perimeter of the material void and stitched. A sample scan image is shown in Figure 48. The scan results revealed a clear, asymmetrical, central material void with cells evenly distributed along its perimeter.

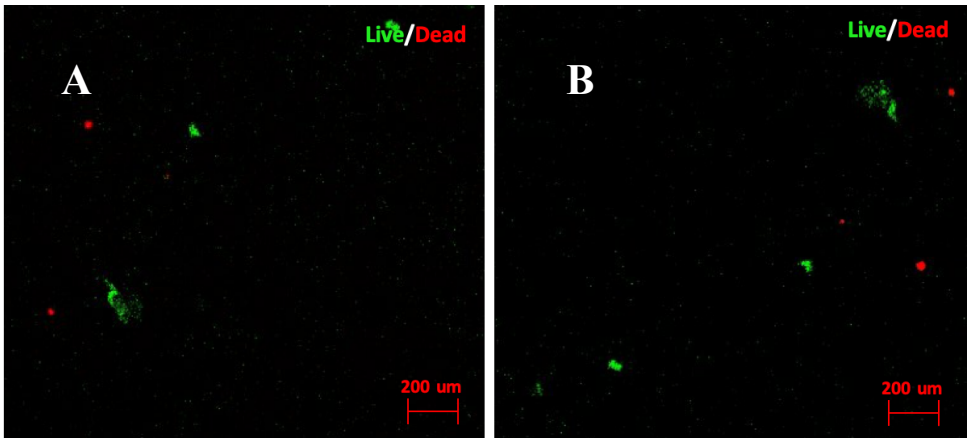

Figure 47: Cell viability for non-injected 30% PPG control (A) and for injected 30% PPG hydrogel (B). Injections were delivered at a driving pressure of 275 kPa and a volume of 0.1 mL.

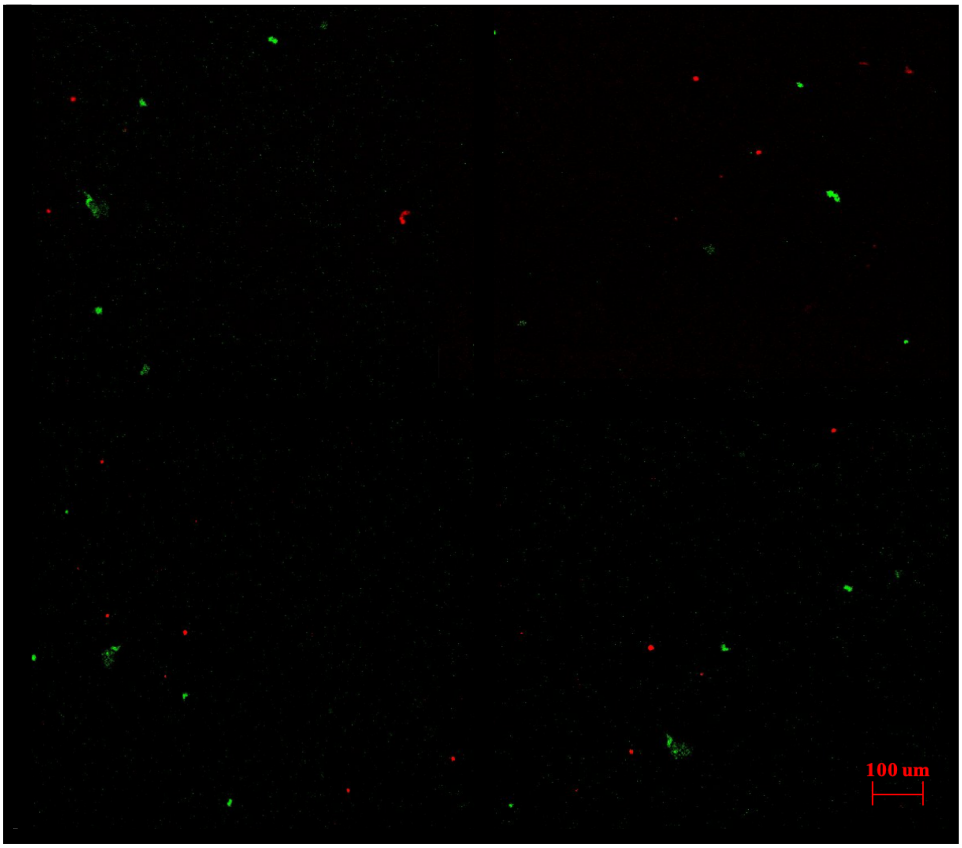

Figure 48: Tile scan of injected PPG hydrogel depicting the total injection site. The figure is composed of 12 individual images, encompassing a 0.25 mm^2 area each, arranged in a 4x3 grid.

The cell viability for the control, needle injection, and NFLJI samples are shown in Table 13. The control sample exhibited a cell viability of 97% ± 2. The needle injection and NFLJI samples supported cell viability of 71% ± 12 and 65% ± 15. The average needle injection cell viability was 1.1x larger than needle-free injection.

Table 13: Cell viabilities of the control, needle injected hydrogel, and needle-free injected hydrogel samples

Sample	**Cell Viability (%)**
Control	97 ± 2
Needle Injection	71% ± 12
Needle-free Injection	65% ± 15

5 DISCUSSION

Research was conducted to better understand the dynamic, morphological, and biological response elicited by needle and needle-free injection in tissue. In order to conduct this research, a porous PPG hydrogel was used. The hydrogel was designed to mimic native vocal fold tissue and to serve as an in-vitro platform for injection. The dynamic, morphological, and cellular response elicited by each technique was assessed at various parameters. Study results contributed to the overall understanding of needle and needle-free injection and their ability to deliver vocal fold injections.

5. 1 HYDROGEL SCAFFOLD CHARACTERIZATION

Testing was conducted to mechanically characterize each PPG hydrogel composition. The results showed that a smaller PEG concentration led to a hydrogel of greater stiffness, elasticity, and toughness. The link between material mechanics and PEG could be explained by the degree of porosity. SEM imaging confirmed that a higher PEG concentration led to a more prominent porous network, as more material per unit volume was removed during washing. The more pores, the more "damage initiation sites", and the less resistant the material to deformation during loading and fracture [68, 69]. In addition to regulating mechanical properties, the porosity impacted liquid dispersion, as injection into the 30% PPG hydrogel most closely matched in-vivo conditions. Pores effected liquid flow through their ability to merge and separate fluid streams [70, 71]. As a result, a greater porosity provided more space for the injected liquid to spread and occupy, recreating a more realistic injection profile [72]. The ability to precisely tune the hydrogel's properties via PEG concentration demonstrated its appropriateness for this study.

Overall, the 30% PPG hydrogel was the composition most similar to native oral mucosa tissue. Although the 10% gel composition best matched fracture toughness, the 30% composition better matched storage modulus values and tissue liquid dispersion. Future work should look to optimize the 30% PPG hydrogel's toughness without sacrificing its porosity and storage modulus. The ability to integrate a double network into the existing 30% PPG composition might offer a potential solution. A double network hydrogel increases material toughness through stress redistribution over two polymer networks [29, 73, 74].

5. 2 Needle Dynamics and Morphological Response

A needle insertion force vs time history was compared to a needle injection history. The needle insertion history maintained a constant injection force over the entire injection duration, while the needle injection history experienced a force drop corresponding to rapid liquid expansion. This result could be explained by hydrodynamic pressure and the effects of needle lubrication. As the injection was delivered, fluid accumulated around the needle tip and the hydrodynamic pressure exerted on the surrounding material increased. Rapid fluid expansion occurred once the fluid's hydrodynamic pressure exceeded the stagnation pressure, relieving the material of its pressure and reducing friction through lubrication. Future work is needed to verify the appropriateness of the PPG gel by investigating whether or not rapid fluid expansion occurs in-vitro too. If not, the hydrogel's pore size, concentration, and distribution should be adjusted to reduce the extent of hydrodynamic build-up such that the liquid is able to gradually disperse.

Needle injection was explored at various parameters. General findings concluded that the force of needle insertion and removal were significantly larger than the force of injection across all parameters. This finding indicated that the needle's kinematic motion, specifically travel into and out of the material, contributed more to the force of injection than the liquid itself. It was then determined that needle-injected fluid profile grew in depth as injection volume, insertion rate, and injection rate increased. It is speculated that increasing liquid volume may have led to a deeper injection as the large fluid mass was required to spread in all directions. It is predicted that increasing injection and insertion deepened the injection by delivering the liquid with greater vertical momentum and by creating a sharply sliced vertical channel for the liquid to travel along. Both occurrences prevented the fluid from spreading laterally. Finally, parameter-specific results were investigated to better understand the key factors of insertion, injection, and removal

force. The findings concluded that 1) the force of needle insertion was governed by friction and needle contact area, 2) the injection force was dictated by hydrodynamic pressure, and 3) the force of removal was dictated by the degree of lubrication. Clinicians can use this knowledge to reduce the force of needle injection. Small, bevel-tipped needles should be used at low injection rates. The hydrodynamic pressure and friction should be addressed through needle lubrication and needle tip redesign.

5. 3 Needle-free Dynamics and Morphological Response

The force time history of needle-free injection reached a maximum force, representing liquid penetration, that dissipated exponentially in a vibrational manner. The average force and time duration of NFLJI was 18x larger and 20x smaller than needle injection. This result could be explained by the needle-free device's powerful driving pressure, as fluid was delivered strongly enough to penetrate the tissue without a metal tool. Future work should look to better understand the vibrational behaviour of NFLJI. It was previously hypothesized that vibrations were derived from the homogeneity of a non-porous material [54]. The current study results contradict this theory, as vibrations were still observed within a porous material. This finding suggests that the vibrations instead reflect the powerful and unconstrained manner in which liquid is delivered. The vibrations may additionally reflect the volume of liquid remaining in the hydrogel after injection, as ringing dissipated most quickly for injections exceeding 40 mm.

The average depth and width of NFLJI was 1.9x and 1.72x greater than needle injection. The fluid dispersion profiles differed between techniques as the needle-free injection resembled a long shaft with a region of deep liquid deposition, rather than spherical body. The increased

depth of NFLJI was likely generated by the fluid's pressure. Once the fluid jet's force became equivalent to the stagnation pressure, the remaining liquid was deposited at a lower force and able to expand radially. This result supported previous findings that inertial effects are more influential at the start of injection, allowing the liquid to penetrate deeply, followed by viscous dissipation at the end of injection [43]. Tearing observed with high volume NFLJI injection likely resulted from the driving pressure being too small to confine the large liquid volume to a thin penetration stream, leading to unconfined and turbulent fluid delivery.

5. 4 Needle and Needle-free Injection Biological Response

The biological response of the hydrogel to needle and needle-free injection was analyzed. Although the average cell viability was 1.1x greater for needle injection, the two techniques were generally comparable. However, the size of injection void varied based on penetration duration and mechanism, as needle-free injection eroded the material rather than displacing it. The creation of a large material void, and thus the obliteration of more cells, reflected the increased damage experienced during needle-free injection. This finding supported the relationship between penetration strength, injection duration, and irreversible tissue damage [72]. Future work should investigate cell viability at different injection depths, as the current results only reflect cell viability at the most superficial layer. Investigating the cell viability at points of maximum fluid width would provide valuable insight regarding the effect of liquid dispersion on cell populations. In addition, future work should identify techniques to increase cell density within the hydrogel. The results showed that biocompatibility hydrogel samples had a greater cell density than the injection samples. Since the biocompatibility hydrogel samples were imaged in their original petri dishes, it is likely that cells attached to the dish were imaged alongside

those integrated within the gel. Future work should identify techniques to increase cell density within the hydrogel by minimizing their attachment to the petri dish.

5. 5 Clinical Implications and Future Work

Overall, needle and needle-free injection differed greatly in terms of force, duration, and injection depth. This finding could be used to explain patient experiences with needle-free injection. First, a greater occurrence of occasional bleeding and bruising has been clinically experienced with NFLJI. This behaviour could be attributed to the forceful and unconfined nature of needle-free injection. Since needle-free delivered fluid was not precisely deposited by a tool, the force of injection and dispersion profile varied more than with needle injection, explaining the occasional and inconsistent occurrence of tissue disturbance. It is predicted that bleeding and bruising occurred when the injection penetrated deep blood vessels and nerves [38]. Findings suggested that needle injection was more painful than NFLJI. This result was explained by the increased duration of needle injection, confirming previous work suggesting that pain is a temporal rather than dynamic feature of injection [54].

Finally, the needle and needle-free injection results assessed their appropriateness for vocal fold injection. Both techniques were successful at delivering solution to the vocal fold-mimicking hydrogel. However, injections delivered by needle exercised a higher degree of control due to their reduced force and increased duration. The degree of control, dictated by the user's ability to fine tune the injection and insertion rate, ensured that the fluid was delivered slowly enough to avoid penetrating surrounding tissue. In addition, the width of the needle injection confirmed its better suitability for vocal fold injection, as clinicians recommend using large gauge needles for sensitive, superficial application sites [10].

Several changes should be implemented to adapt needle-free injection for the treatment of vocal fold disorders. Needle-free injection was most similar to needle injection at low driving pressures and liquid volumes. The liquid volume required for vocal fold injection is dictated by the clinician and should be treated as a given fixed value. As a result, the driving force of needle-free injection should be reduced to decrease injection depth. Ideally, a threshold pressure capable of puncturing the tissue without leading to deep penetration would be identified. A smaller nozzle diameter could also be employed to match that of a desired needle gauge while the vibrational force elicited by NFLJI be better understood to ensure that it does harm the patient.

Next steps should additionally look to integrate medically relevant factors into the experiment. Injections should be delivered using clinically relevant materials, such as collagen, to ensure accurate dispersion given the effects of liquid viscosity on spreading in a porous medium [43]. Additionally, injections should be delivered by hand. While creating reproducible results, the current apparatus did not reflect the fluctuating pressure produced by a clinician when pushing on the needle's plunger or injector's trigger. Delivering injections by hand would provide further insight regarding the delivery depth accuracy achieved with needle and NFLJI.

Next, future work should look to add increased complexity to the hydrogel scaffold. The scaffold should be engineered to incorporate blood vessels and masses within the tissue, as well as an immune response to indicate the presence of swelling [75]. Swelling is of particular interest given its link to pain [76]. Finally, a scaffold representing unhealthy LP should be created by altering the PEG concentration, as the stiffening of diseased tissue is often treated through

material injection. It is hypothesized that NFLJI would be more appropriate for delivering injections to diseased hydrogels, as a stiffer material would withstand and resist large penetrative forces more effectively.

6 CONCLUSIONS AND SUGGESTIONS FOR FUTURE WORK

The objective of the research was to contribute to the knowledge of needle and needle-free injection by investigating the dynamic, morphological, and cellular response elicited by each. A porous vocal fold mimicking phantom was engineered as an experimental platform. The phantom added novelty to the study, as most in-vitro experiments have been limited by their application of a non-porous hydrogel or cadaver. Although the ability to precisely tune the phantom's porosity and mechanical properties via PEG concentration demonstrated its appropriateness for the study, future work should look to improve its ability to match the vocal fold's fracture toughness. In comparing needle and needle-free injection, both techniques varied in terms of the dynamic, morphological, and cellular response they elicited. The average force and time duration of NFLJI was 18x larger and 20x smaller than needle injection. Needle injection was characterized by periods of needle insertion, injection, and removal while needle-free injection was characterized by a vibrational force that dissipated exponentially. The average depth and width of NFLJI was 1.9x and 1.72x greater than needle injection. Needle injection expanded from a point source at the needle's tip while needle-free liquid dispersion took the shape of a long shaft. Variation in injection depth and width, as well as the presence of material tearing, reflected force and duration differences between injection techniques. The forceful and unconfined nature of NFLJI served as a promising explanation for reported occurrences of occasional patient bleeding, bruising, and reduced pain. While the cell viability of the two injection techniques were comparable, the larger

material void left by NFLJI indicated a link between penetration strength and irreversible tissue damage. Overall, the study results suggested that needle injection was a more appropriate technique for vocal fold delivery given the higher degree of control achieved by its reduced force and increased duration. In order to make the needle-free injector more suitable for this application, it is suggested that the device's driving force be reduced to a threshold pressure capable of puncturing the tissue without leading to deep liquid penetration. It is additionally suggested that a smaller nozzle be implemented to better match the width of needle injection and that the vibrational force elicited by NFLJI be addressed. Once accomplished, medically relevant factors should be integrated into the experiment to increase the complexity of the phantom. The current results, coupled with future study directions, will work towards improving health outcomes by providing greater insight on the current and potential capabilities of each injection technique.

REFERENCES

[1] A. K. Miri, "Mechanical characterization of vocal fold tissue: a review study," *J Voice,* vol. 28, no. 6, pp. 657-67, Nov 2014, doi: 10.1016/j.jvoice.2014.03.001.

[2] E. L. Kelley, R. H. Smith, G. Corcoran, S. Nygren, M. V. Jacoski, and A. Fernandes, "Advances in subcutaneous injections: PRECISE II: a study of safety and subject preference for an innovative needle-free injection system," *Drug Deliv,* vol. 28, no. 1, pp. 1915-1922, Dec 2021, doi: 10.1080/10717544.2021.1976309.

[3] P. Szmuk, E. Szmuk, and T. Ezri, "Use of needle-free injection systems to alleviate needle phobia and pain at injection," *Expert Review of Pharmacoeconomics & Outcomes Research,* vol. 5, no. 4, pp. 467-477, 2005/08/01 2005, doi: 10.1586/14737167.5.4.467.

[4] J. Baxter and S. Mitragotri, "Jet-induced skin puncture and its impact on needle-free jet injections: experimental studies and a predictive model," *J Control Release,* vol. 106, no. 3, pp. 361-73, Sep 2 2005, doi: 10.1016/j.jconrel.2005.05.023.

[5] M. Saran, B. Georgakopoulos, and B. Bordoni, "Anatomy, Head and Neck, Larynx Vocal Cords," in *StatPearls*. Treasure Island (FL), 2023.

[6] "Morphology of Vocal Fold Mucosa : Histology to Genomics," 2010.

[7] R. W. Chan and I. R. Titze, "Viscoelastic shear properties of human vocal fold mucosa: measurement methodology and empirical results," *J Acoust Soc Am,* vol. 106, no. 4 Pt 1, pp. 2008-21, Oct 1999, doi: 10.1121/1.427947.

[8] I. Klepacek, D. Jirak, M. Duskova Smrckova, O. Janouskova, and T. Vampola, "The Human Vocal Fold Layers. Their Delineation Inside Vocal Fold as a Background to Create 3D Digital and Synthetic Glottal Model," *Journal of Voice,* vol. 30, no. 5, pp. 529-537, 2016/09/01/ 2016, doi: https://doi.org/10.1016/j.jvoice.2015.08.004.

[9] M. Hirano, Y. Kakita, K. Ohmaru, and S. Kurita, "Structure and Mechanical Properties of the Vocal Fold1 1A portion of this article was presented at the Vocal Fold Physiology Conference, Kurume, Japan, in January 1980," in *Speech and Language*, vol. 7, N. J. Lass Ed.: Elsevier, 1982, pp. 271-297.

[10] H. v. L. a. R. H. Ossoff, *Operative Techniques in Laryngology Forewords*: Springer, 2008.

[11] S. S. Teller *et al.*, "High-Frequency Viscoelastic Shear Properties of Vocal Fold Tissues: Implications for Vocal Fold Tissue Engineering," *Tissue Engineering Part A,* vol. 18, no. 19-20, pp. 2008-2019, 2012/10/01 2012, doi: 10.1089/ten.tea.2012.0023.

[12] J. Jiang, E. Lin, and D. G. Hanson, "Vocal fold physiology," *Otolaryngol Clin North Am,* vol. 33, no. 4, pp. 699-718, Aug 2000, doi: 10.1016/s0030-6665(05)70238-3.

[13] W. Jiang, X. Zheng, and Q. Xue, "Influence of vocal fold cover layer thickness on its vibratory dynamics during voice production," *J Acoust Soc Am,* vol. 146, no. 1, p. 369, Jul 2019, doi: 10.1121/1.5116567.

[14] G. R. Dion *et al.*, "Functional assessment of the ex vivo vocal folds through biomechanical testing: A review," *Materials Science and Engineering: C,* vol. 64, pp. 444-453, 2016/07/01/ 2016, doi: https://doi.org/10.1016/j.msec.2016.04.018.

[15] W. H. Tseng, C. C. Chang, T. L. Yang, and T. Y. Hsiao, "Estimating vocal fold stiffness: Using the relationship between subglottic pressure and fundamental frequency of phonation as an analog," (in eng), *Clin Otolaryngol,* vol. 45, no. 1, pp. 40-46, Jan 2020, doi: 10.1111/coa.13463.

[16] S. Takahashi *et al.*, "Comparison of therapeutic effects of steroid injection by benign vocal fold lesion type," *Acta Otolaryngol,* vol. 141, no. 11, pp. 1005-1013, Nov 2021, doi: 10.1080/00016489.2021.1995895.

[17] B. Rousseau *et al.*, "Characterization of chronic vocal fold scarring in a rabbit model," *Journal of Voice,* vol. 18, no. 1, pp. 116-124, 2004/03/01/ 2004, doi: https://doi.org/10.1016/j.jvoice.2003.06.001.

[18] S. L. Thibeault, S. D. Gray, D. M. Bless, R. W. Chan, and C. N. Ford, "Histologic and Rheologic Characterization of Vocal Fold Scarring," *Journal of Voice,* vol. 16, no. 1, pp. 96-104, 2002/03/01/ 2002, doi: https://doi.org/10.1016/S0892-1997(02)00078-4.

[19] E. Goodyer, N. V. Welham, S. H. Choi, M. Yamashita, and S. H. Dailey, "The shear modulus of the human vocal fold in a transverse direction," *J Voice,* vol. 23, no. 2, pp. 151-5, Mar 2009, doi: 10.1016/j.jvoice.2007.09.006.

[20] P. S. Mallur and C. A. Rosen, "Vocal fold injection: review of indications, techniques, and materials for augmentation," (in eng), *Clin Exp Otorhinolaryngol,* vol. 3, no. 4, pp. 177-82, Dec 2010, doi: 10.3342/ceo.2010.3.4.177.

[21] S. A. Klemuk and I. R. Titze, "Viscoelastic Properties of Three Vocal-Fold Injectable Biomaterials at Low Audio Frequencies," *The Laryngoscope,* vol. 114, no. 9, pp. 1597-1603, 2004, doi: https://doi.org/10.1097/00005537-200409000-00018.

[22] J. Yin and Z. Zhang, "The influence of thyroarytenoid and cricothyroid muscle activation on vocal fold stiffness and eigenfrequencies," *The Journal of the Acoustical Society of America,* vol. 133, no. 5, pp. 2972-2983, 2013, doi: 10.1121/1.4799809.

[23] D. K. Chhetri, Z. Zhang, and J. Neubauer, "Measurement of Young's modulus of vocal folds by indentation," *J Voice,* vol. 25, no. 1, pp. 1-7, Jan 2011, doi: 10.1016/j.jvoice.2009.09.005.

[24] E. Goodyer, S. Hemmerich, F. Muller, J. B. Kobler, and M. Hess, "The shear modulus of the human vocal fold, preliminary results from 20 larynxes," *Eur Arch Otorhinolaryngol,* vol. 264, no. 1, pp. 45-50, Jan 2007, doi: 10.1007/s00405-006-0133-8.

[25] D. K. Chhetri, G. S. Berke, A. Lotfizadeh, and E. Goodyer, "Control of vocal fold cover stiffness by laryngeal muscles: a preliminary study," *Laryngoscope,* vol. 119, no. 1, pp. 222-7, Jan 2009, doi: 10.1002/lary.20031.

[26] Z. Zhang, H. Samajder, and J. L. Long, "Biaxial mechanical properties of human vocal fold cover under vocal fold elongation," *J Acoust Soc Am,* vol. 142, no. 4, p. EL356, Oct 2017, doi: 10.1121/1.5006205.

[27] Q. T. Tran, G. S. Berke, B. R. Gerratt, and J. Kreiman, "Measurement of Young's modulus in the in vivo human vocal folds," *Ann Otol Rhinol Laryngol,* vol. 102, no. 8 Pt 1, pp. 584-91, Aug 1993, doi: 10.1177/000348949310200803.

[28] D. Taylor, N. O'Mara, E. Ryan, M. Takaza, and C. Simms, "The fracture toughness of soft tissues," (in eng), *J Mech Behav Biomed Mater,* vol. 6, pp. 139-47, Feb 2012, doi: 10.1016/j.jmbbm.2011.09.018.

[29] S. Taheri *et al.*, "Injectable, Pore-Forming, Perfusable Double-Network Hydrogels Resilient to Extreme Biomechanical Stimulations," *Adv Sci (Weinh),* vol. 9, no. 2, p. e2102627, Jan 2022, doi: 10.1002/advs.202102627.

[30] T. Azar and V. Hayward, "Estimation of the Fracture Toughness of Soft Tissue from Needle Insertion," in *Biomedical Simulation*, Berlin, Heidelberg, F. Bello and P. J. E. Edwards, Eds., 2008// 2008: Springer Berlin Heidelberg, pp. 166-175.

[31] M. O-Leary, C. Backes, T. Washio, K. Yoshinaka, and A. Okamura, *Robotic needle insertion: Effects of friction and needle geometry*. 2003, pp. 1774-1780.

[32] R. Craig. "A history of syringes and needles." The University of Queensland. https://medicine.uq.edu.au/blog/2018/12/history-syringes-and-needles (accessed.

[33] H. Kim, H. Park, and S. J. Lee, "Effective method for drug injection into subcutaneous tissue," *Scientific Reports,* vol. 7, no. 1, p. 9613, 2017/08/29 2017, doi: 10.1038/s41598-017-10110-w.

[34] J. Schramm and S. Mitragotri, "Transdermal drug delivery by jet injectors: energetics of jet formation and penetration," *Pharm Res,* vol. 19, no. 11, pp. 1673-9, Nov 2002, doi: 10.1023/a:1020753329492.

[35] A. D. Ravi, D. Sadhna, D. Nagpaal, and L. Chawla, "Needle free injection technology: A complete insight," *Int J Pharm Investig,* vol. 5, no. 4, pp. 192-9, Oct-Dec 2015, doi: 10.4103/2230-973X.167662.

[36] A. Mohizin and J. K. Kim, "Current engineering and clinical aspects of needle-free injectors: A review," *Journal of Mechanical Science and Technology,* vol. 32, no. 12, pp. 5737-5747, 2018/12/01 2018, doi: 10.1007/s12206-018-1121-9.

[37] G. R. Hughes, "The use of the hypospray in the treatment of minor orthopaedic conditions," (in eng), *Proc R Soc Med,* vol. 62, no. 6, p. 577, Jun 1969.

[38] S. Mitragotri, "Current status and future prospects of needle-free liquid jet injectors," *Nat Rev Drug Discov,* vol. 5, no. 7, pp. 543-8, Jul 2006, doi: 10.1038/nrd2076.

[39] S. Mitragotri, "Immunization without needles," *Nature Reviews Immunology,* vol. 5, no. 12, pp. 905-916, 2005/12/01 2005, doi: 10.1038/nri1728.

[40] M. Dukare and R. Saudagar, "NEEDLE-FREE INJECTION SYSTEM," *International Journal of Current Pharmaceutical Research,* vol. 10, p. 17, 03/15 2018, doi: 10.22159/ijcpr.2018v10i2.25885.

[41] Y. Zhu, C. Kang, W. Cai, and C. Huang, "Drug injection and dispersion characteristics of an air-powered needle-free injector," *Med Eng Phys,* vol. 109, p. 103906, Nov 2022, doi: 10.1016/j.medengphy.2022.103906.

[42] N. Kojic, P. Goyal, C. H. Lou, and M. J. Corwin, "An Innovative Needle-free Injection System: Comparison to 1 ml Standard Subcutaneous Injection," (in eng), *AAPS PharmSciTech,* vol. 18, no. 8, pp. 2965-2970, Nov 2017, doi: 10.1208/s12249-017-0779-0.

[43] L. Oyarte Gálvez, M. Brió Pérez, and D. Fernández Rivas, "High speed imaging of solid needle and liquid micro-jet injections," *Journal of Applied Physics,* vol. 125, no. 14, 2019, doi: 10.1063/1.5074176.

[44] H. S. Han *et al.*, "Mechanism and clinical applications of needle-free injectors in dermatology: Literature review," *J Cosmet Dermatol,* vol. 20, no. 12, pp. 3793-3801, Dec 2021, doi: 10.1111/jocd.14047.

[45] M. Moradiafrapoli and J. O. Marston, "High-speed video investigation of jet dynamics from narrow orifices for needle-free injection," *Chemical Engineering Research and Design,* vol. 117, pp. 110-121, 2017/01/01/ 2017, doi: https://doi.org/10.1016/j.cherd.2016.10.023.

[46] J. R. Schramm-Baxter and S. Mitragotri, "Investigations of needle-free jet injections," *Conf Proc IEEE Eng Med Biol Soc,* vol. 2004, pp. 3543-6, 2004, doi: 10.1109/IEMBS.2004.1403996.

[47] T. R. Kwon *et al.*, "Needle-free jet injection of hyaluronic acid improves skin remodeling in a mouse model," *Eur J Pharm Biopharm,* vol. 105, pp. 69-74, Aug 2016, doi: 10.1016/j.ejpb.2016.05.014.

[48] P. G. Agache, C. Monneur, J. L. Leveque, and J. De Rigal, "Mechanical properties and Young's modulus of human skin in vivo," *Arch Dermatol Res,* vol. 269, no. 3, pp. 221-32, 1980, doi: 10.1007/BF00406415.

[49] T. Kato *et al.*, "Mechanics of the injected pulsejet into gelatin gel and evaluation of the effect by puncture and crack generation and growth," *Journal of Applied Physics,* vol. 116, no. 7, 2014, doi: 10.1063/1.4893175.

[50] J. Schramm-Baxter and S. Mitragotri, "Needle-free jet injections: dependence of jet penetration and dispersion in the skin on jet power," *Journal of Controlled Release,* vol. 97, no. 3, pp. 527-535, 2004/07/07/ 2004, doi: https://doi.org/10.1016/j.jconrel.2004.04.006.

[51] J. Schramm-Baxter and S. Mitragotri, "Needle-free jet injections: dependence of jet penetration and dispersion in the skin on jet power," *J Control Release,* vol. 97, no. 3, pp. 527-35, Jul 7 2004, doi: 10.1016/j.jconrel.2004.04.006.

[52] J. Bennett, F. Nichols, M. Rosenblum, and J. Condry, "Subcutaneous administration of midazolam: a comparison of the Bioject jet injector with the conventional syringe and needle," *J Oral Maxillofac Surg,* vol. 56, no. 11, pp. 1249-54, Nov 1998, doi: 10.1016/s0278-2391(98)90601-2.

[53] S. J. Hollingsworth, K. Hoque, D. Linnard, D. G. Corry, and S. G. Barker, "Delivery of low molecular weight heparin for prophylaxis against deep vein thrombosis using a novel, needle-less injection device (J-Tip)," *Ann R Coll Surg Engl,* vol. 82, no. 6, pp. 428-31, Nov 2000. [Online]. Available: https://www.ncbi.nlm.nih.gov/pubmed/11103165.

[54] A. Henley *et al.*, *Injection Dynamics Of Drug Delivery Via Needle-Free Pneumatic Jet Injection*. 2021.

[55] Y. Nanda Kumar *et al.*, "Development of Tough Hydrogel Phantoms to Mimic Fibrous Tissue for Focused Ultrasound Therapies," (in eng), *Ultrasound Med Biol,* vol. 48, no. 9, pp. 1762-1777, Sep 2022, doi: 10.1016/j.ultrasmedbio.2022.05.002.

[56] C. Nhan, J. Chankowsky, C. Torres, and L.-M. Boucher, "Creating Low-Cost Phantoms for Needle Manipulation Training in Interventional Radiology Procedures," *RadioGraphics,* vol. 41, no. 4, pp. 1230-1242, 2021/07/01 2021, doi: 10.1148/rg.2021200133.

[57] Y. H. Kim, "Ultrasound Phantoms to Protect Patients from Novices," (in eng), *Korean J Pain,* vol. 29, no. 2, pp. 73-7, Apr 2016, doi: 10.3344/kjp.2016.29.2.73.

[58] M. Navarro-Lozoya, M. S. Kennedy, D. Dean, and J. I. Rodriguez-Devora, "Development of Phantom Material that Resembles Compression Properties of Human Brain Tissue for Training Models," (in eng), *Materialia (Oxf),* vol. 8, Dec 2019, doi: 10.1016/j.mtla.2019.100438.

[59] C. J. Taylor, G. J. Tarbox, B. D. Bolster, Jr., N. K. Bangerter, and S. L. Thomson, "Magnetic resonance imaging-based measurement of internal deformation of vibrating

vocal fold models," (in eng), *J Acoust Soc Am,* vol. 145, no. 2, p. 989, Feb 2019, doi: 10.1121/1.5091009.

[60] A. D. Maxwell, T. Y. Wang, L. Yuan, A. P. Duryea, Z. Xu, and C. A. Cain, "A tissue phantom for visualization and measurement of ultrasound-induced cavitation damage," (in eng), *Ultrasound Med Biol,* vol. 36, no. 12, pp. 2132-43, Dec 2010, doi: 10.1016/j.ultrasmedbio.2010.08.023.

[61] D. Ferri-Angulo *et al.*, "Versatile fiber-reinforced hydrogels to mimic the microstructure and mechanics of human vocal-fold upper layers," *Acta Biomaterialia,* vol. 172, pp. 92-105, 2023/12/01/ 2023, doi: https://doi.org/10.1016/j.actbio.2023.09.035.

[62] R. W. Chan, "Measurements of vocal fold tissue viscoelasticity: approaching the male phonatory frequency range," *J Acoust Soc Am,* vol. 115, no. 6, pp. 3161-70, Jun 2004, doi: 10.1121/1.1736272.

[63] ThermoFisher. "Useful Numbers for Cell Culture." (accessed.

[64] M. Nozawa *et al.*, "Intracordal injection therapy for vocal fold scarring: Steroid versus basic fibroblast growth factor," *Laryngoscope Investig Otolaryngol,* vol. 7, no. 5, pp. 1465-1473, Oct 2022, doi: 10.1002/lio2.881.

[65] P. Woo and T. Murry, "Short-Term Voice Improvement after Repeated Office-Based Platelet-Rich Plasma PRP Injection in Patients with Vocal Fold Scar, Sulcus, and Atrophy," (in eng), *J Voice,* Mar 18 2021, doi: 10.1016/j.jvoice.2021.02.022.

[66] S. Hirano, Y. Sugiyama, M. Kaneko, S. Mukudai, S. Fuse, and K. Hashimoto, "Intracordal Injection of Basic Fibroblast Growth Factor in 100 Cases of Vocal Fold Atrophy and Scar," *Laryngoscope,* vol. 131, no. 9, pp. 2059-2064, Sep 2021, doi: 10.1002/lary.29200.

[67] S.-H. Lee *et al.*, "Local Steroid Injection via the Cricothyroid Membrane in Patients With a Vocal Nodule," *Archives of Otolaryngology–Head & Neck Surgery,* vol. 137, no. 10, pp. 1011-1016, 2011, doi: 10.1001/archoto.2011.168.

[68] R. Perkins, W. Yang, Y. Liu, L. Chen, and C. Yenusah, *Finite Element Analysis of the Effect of Porosity on the Plasticity and Damage Behavior of Mg AZ31 and Al 6061 T651 Alloys*. 2019.

[69] A. Y. Al-Maharma, S. P. Patil, and B. Markert, "Effects of porosity on the mechanical properties of additively manufactured components: a critical review," *Materials Research Express,* vol. 7, no. 12, p. 122001, 2020/12/02 2020, doi: 10.1088/2053-1591/abcc5d.

[70] , "Chapter 2 The Theory of Dispersion in Porous Media," in *Developments in Water Science*, vol. 4, J. J. Fried Ed.: Elsevier, 1975, pp. 5-46.

[71] V. Nguyen and D. V. Papavassiliou, "Hydrodynamic Dispersion in Porous Media and the Significance of Lagrangian Time and Space Scales," *Fluids,* vol. 5, no. 2, p. 79, 2020. [Online]. Available: https://www.mdpi.com/2311-5521/5/2/79.

[72] P. Hou, F. Zheng, C. D. Corpstein, L. Xing, and T. Li, "Multiphysics Modeling and Simulation of Subcutaneous Injection and Absorption of Biotherapeutics: Sensitivity Analysis," (in eng), *Pharm Res,* vol. 38, no. 6, pp. 1011-1030, Jun 2021, doi: 10.1007/s11095-021-03062-4.

[73] T. Lu, W. Zhang, and Y. Zhou, "6 - Fatigue of hydrogels," in *The Mechanics of Hydrogels*, H. Li and V. Silberschmidt Eds.: Woodhead Publishing, 2022, pp. 119-138.

[74] H. Xin, "Double-Network Tough Hydrogels: A Brief Review on Achievements and Challenges," (in eng), *Gels,* vol. 8, no. 4, Apr 18 2022, doi: 10.3390/gels8040247.

[75] A. Mohizin, J. H. Imran, K. S. Lee, and J. K. Kim, "Dynamic interaction of injected liquid jet with skin layer interfaces revealed by microsecond imaging of optically cleared ex vivo skin tissue model," *Journal of Biological Engineering,* vol. 17, no. 1, p. 15, 2023/02/27 2023, doi: 10.1186/s13036-023-00335-x.

[76] D. W. Kang, D. A. Oh, G. Y. Fu, J. M. Anderson, and M. L. Zepeda, "Porcine model to evaluate local tissue tolerability associated with subcutaneous delivery of protein," (in eng), *J Pharmacol Toxicol Methods,* vol. 67, no. 3, pp. 140-7, May-Jun 2013, doi: 10.1016/j.vascn.2013.01.011.